Photoionization of helium by attosecond pulses: Extraction of spectra from correlated wave functions

Luca Argenti, Renate Pazourek, Johannes Feist, Stefan Nagele, Matthias Liertzer, Emil Persson, Joachim Burgdörfer, and Eva Lindroth

Photoionization of helium by attosecond pulses: extraction of spectra from correlated wave functions

Luca Argenti,[1, *] Renate Pazourek,[2] Johannes Feist,[3, 4] Stefan Nagele,[2]
Matthias Liertzer,[2] Emil Persson,[2] Joachim Burgdörfer,[2] and Eva Lindroth[5]

[1]*Departamento de Química, Módulo 13, Universidad Autónoma de Madrid, 28049 Madrid, Spain, EU*
[2]*Institute for Theoretical Physics, Vienna University of Technology, 1040 Vienna, Austria, EU*
[3]*ITAMP, Harvard-Smithsonian Center for Astrophysics, Cambridge, Massachussetts 02138, USA*
[4]*Departamento de Física Teórica de la Materia Condensada,*
Universidad Autónoma de Madrid, E-28049 Madrid, Spain
[5]*Department of Physics, Stockholm University, AlbaNova University Center, SE-106 91 Stockholm, Sweden, EU*
(Dated: April 15, 2013)

We investigate the photoionization spectrum of helium by attosecond XUV pulses both in the spectral region of doubly excited resonances as well as above the double ionization threshold. In order to probe for convergence, we compare three techniques to extract photoelectron spectra from the wavepacket resulting from the integration of the time-dependent Schrödinger equation in a finite-element discrete variable representation basis. These techniques are: projection on products of hydrogenic bound and continuum states, projection onto multi-channel scattering states computed in a B-spline close-coupling basis, and a technique based on exterior complex scaling (ECS) implemented in the same basis used for the time propagation. These methods allow to monitor the population of continuum states in wavepackets created with ultrashort pulses in different regimes. Applications include photo cross sections and anisotropy parameters in the spectral region of doubly excited resonances, time-resolved photoexcitation of autoionizing resonances in an attosecond pump-probe setting, and the energy and angular distribution of correlated wavepackets for two-photon double ionization.

PACS numbers: 31.15.ac, 32.80.Fb, 32.80.Rm, 32.80.Zb

I. INTRODUCTION

During the last decade, two transformational experimental techniques, high harmonic generation [1] and x-ray free electron lasers [2], have given access to femtosecond and sub-femtosecond intense light pulses in the XUV and soft x-ray energy range, thus opening the way to time resolved studies of the correlated motion of electrons in atoms and molecules on their characteristic time-scale [3–10]. These new techniques can be used not only to monitor the electronic motion but also to steer it [11, 12]. This latter capability offers the perspective of controlling dynamics at the femtosecond and sub-femtosecond timescale, such as electronic dynamics in atoms [13, 14], molecules [15–17], and solids [18], and eventually also nuclear dynamics such as fast proton migration [19].

The interpretation of experiments on attosecond dynamics, however, faces a number of difficulties and requires guidance by theory. First, sub-femtosecond pulses typically excite the target to a coherent superposition of states above the ionization threshold and across a wide range of energies. As a consequence, several different ionization regimes such as multiply excited autoionizing states, multichannel single ionization states and, possibly, multiple ionization states, are accessed at the same time. Second, in common pump-probe schemes [15], the

strong few-cycle IR-probe pulse that follows an attosecond weak XUV-pump pulse gives rise to electronic dynamics that unfolds on a very short time-scale through non-perturbative stages, e.g. tunneling, over-the-barrier ionization, and Rabi oscillations.

Traditional perturbative approaches [20] are clearly not well suited to describe such dynamical regimes. Moreover, since the duration of compressed IR pulses easily spans just a few [21] or even a single [22] carrier cycle, stationary non-perturbative techniques like those based on the Floquet method [23] cannot be used either. Reliable theoretical predictions for ultrashort processes, therefore, generally require direct integration of the time-dependent Schrödinger equation (TDSE) [14, 24–34]. Such an approach permits to reproduce faithfully the physical process under study. However, it gives rise to a multitude of problems as well. Relevant parts, if not most, of the electron dynamics triggered by sub-femtosecond pulses take place in the ionization continuum. Indeed, typical experiments are designed to monitor the energy and angular distribution of the photoelectrons emerging from the reaction center, e.g., with a velocity map imaging spectrometer [35], or even several photo-fragments in coincidence, e.g., with a reaction microscope [36]. Transient absorption spectroscopy [37], which monitors quasi-bound electronic dynamics, constitutes a notable exception. One of the most prominent problems theory has to face is then how to extract from a numerical simulation, intrinsically limited in both time and space, the relevant asymptotic scattering informa-

tion.

A number of alternative techniques have been used in the past to extract differential distributions of the products of a light-induced reaction from an entangled wave function: spectral analysis of autocorrelation functions [38], analysis of the radial flux at large distances [39], projection of the wavepacket onto products of one-particle functions, e.g., Coulomb functions [26, 32, 40] or Volkov states [28], asymptotic analysis of a monochromatic component of the wavepacket extracted with the resolvent technique [41], surface integration of the monochromatic component of the wave function extracted with a technique based on exterior complex scaling (Berkeley-ECS) [33, 42–44], or projection on scattering states computed on the same basis used to carry out the time propagation [14, 29–31, 40, 45, 46]. Very recently [47, 48] a method that combines the flux analysis at moderate radii with the ECS technique for optical absorption at larger distances was proposed. Implementations for the full Coulomb two-electron problem are, however, not yet available.

In the following, we investigate three of these techniques in more detail for the prototypical three-body system, the helium atom: projection onto products of one-particle functions, projection onto exact scattering states, and the Berkeley-ECS method. For all these techniques, the extraction of asymptotic scattering information takes place in the field-free region after the laser pulse is over. As will be discussed in more detail later, each of these approaches has its strengths and drawbacks making it applicable for different photon energies and pulse durations. By comparing results from complementary methods we are able to assess the convergence of the simulation of dynamical observables that have become accessible by attosecond photoelectron spectroscopy. We will present applications to three sets of benchmark data: i) photoionization cross sections and anisotropy parameters for single ionization of helium in the spectral region of doubly-excited resonances, ii) time-resolved photoionization by an attosecond pump-probe setting in the same spectral domain, and iii) the energy and angular distribution of correlated wavepackets in two-photon ionization by ultrashort pulses above the double ionization threshold.

The article is organized as follows. In section II we briefly review our method of solving the time-dependent Schrödinger equation (TDSE) for helium in its full dimensionality. The method allows to accurately represent the electronic wavepacket generated by (a sequence of) ultrashort light pulses on a grid with a finite spatial domain and for a finite propagation time. Three alternative methods to extract dynamical observables from such wavepackets are introduced and their applicability in different regimes is compared in section III. Applications to three scenarios of current interest are presented in section IV followed by concluding remarks in section V. Additional technical and computational details are given in the appendix. Atomic units are used throughout unless

stated otherwise.

II. PROPAGATION METHOD

Our computational approach (see [32, 49, 50] for a more detailed description) for solving the time-dependent Schrödinger equation for two-electron systems,

$$i\frac{\partial}{\partial t}\Psi(\mathbf{r}_1,\mathbf{r}_2,t) = H\Psi(\mathbf{r}_1,\mathbf{r}_2,t),\qquad(1)$$

is based on a time-dependent close-coupling scheme [51–54] where we expand the angular part of the six-dimensional wave function $\Psi(\mathbf{r}_1,\mathbf{r}_2)$ in coupled spherical harmonics $\mathcal{Y}_{l_1,l_2}^{LM}(\Omega_1,\Omega_2)$.

The interaction of a helium atom with linearly polarized light is described by the Hamiltonian

$$H = H_a + H_{\rm em}^{l,v} = \frac{\hat{\mathbf{p}}_1^2}{2} + \frac{\hat{\mathbf{p}}_2^2}{2} - \frac{2}{r_1} - \frac{2}{r_2} + \frac{1}{|\mathbf{r}_1-\mathbf{r}_2|} + H_{\rm em}^{l,v},\qquad(2)$$

where the interaction with the electromagnetic field in the dipole approximation, $H_{\rm em}^{l,v}$, is either given in *length* or *velocity* gauge. The gauge independence of the physical observables is a necessary condition for the convergence of the numerical solution.

For the discretization of the radial functions $R_{l_1,l_2}^L(r_1,r_2,t)$, we employ a finite-element discrete-variable representation (FEDVR) [55–57]. We divide the radial coordinates into finite elements in each of which the functions R_{l_1,l_2}^L are represented in a local DVR basis with a corresponding Gauss-Lobatto quadrature to ensure the continuity of the wave function at the element boundaries. This method leads to sparse matrix representations of the differential operators and to a diagonal potential matrix (within quadrature accuracy), enabling efficient parallelization.

For the temporal propagation, we employ the short iterative Lanczos (SIL) method [58–60] with adaptive time-step control. The initial He ground state $1^1S(1s^2)$ is obtained by relaxing an arbitrary test function in imaginary time. For an initial $2^1S(1s2s)$ metastable state we directly solve the eigenvalue problem of the field-free Hamiltonian H_a (see Eq. 2) in a small box using the SLEPc library [61]. The radial grid covers a range $[0,r_{\rm max}]$, with typical values of $r_{\rm max} \approx 150$ a.u., although much larger values are possible. The temporal integration extends to a maximum time $t_{\rm max}$ which exceeds at least the pulse length $t_{\rm max} > \tau_p$ ($\tau_p \approx 1600$ as $\simeq 65$ a.u. for $T_{\rm FWHM}$=200 as of a Gaussian intensity envelope) but may be increased much further (up to $t_{\rm max} \approx 8$ fs), as discussed below. At the conclusion of the time propagation, the wavepacket $\Psi(\mathbf{r}_1,\mathbf{r}_2,t_{\rm max})$ contains all accessible scattering information. The extraction of this information on the asymptotic scattering state, i.e., the $t \to \infty$ limit, is a non-trivial numerical task for which we discuss in the following three, partially complementary, techniques.

III.   ALTERNATIVE EXTRACTION METHODS

In order to extract the information on the energy and angular distribution of emergent photofragments, it is crucial to establish a correspondence between the experimental observables and the simulated finite domain wavepacket dynamics. In principle, this is straightforward: Upon conclusion of the electromagnetic pulse, the numerical solution of the TDSE yields the wave function $\Psi(t)$ of the wavepacket. The dynamics of $\Psi(t)$ is then governed by the total field-free atomic Hamiltonian, H_a. The state $\Psi(t)$ is composed of a bound and an unbound part. Let us indicate by Λ the projector on the bound states of H_a, and with $\Psi'(t) = (\mathbb{1} - \Lambda)\Psi(t)$ the unbound part of $\Psi(t)$. The fragments detected are associated with the long-time limit of the unbound component $\Psi'(t)$, which consists of a superposition of unbound eigenstates $\varphi_{\alpha E}$ of the sum of the Hamiltonians of the separated fragments, H_0. The projection amplitudes

$$c_{\alpha E}(t) = \langle \varphi_{\alpha E} \,|\, \Psi'(t) \rangle, \qquad (3)$$

where α designates the collective set of quantum numbers beyond the total energy E, uniquely characterize the final state of the system. These include the fragmentation channel of the target, the asymptotic angular distribution of the photofragments, and their internal quantum numbers (e.g. spin and angular momentum).

The expansion coefficients $c_{\alpha E}(t)$ in (3) may not necessarily converge in the infinite-time limit. In particular, when two or more fragments are charged, the phase of $c_{\alpha E}(t)$ diverges due to the long-range character of the Coulomb field. Notwithstanding this difficulty the probability density $|c_{\alpha E}(t)|^2$ will still converge in the sense of distributions (i.e., when convoluted with a test function) yielding a well-defined asymptotic distribution of the fragments. Hence, the probability distribution $P_\alpha(E)$ for the detection of fragments in channel α and with energy E at the end of the propagation is given by

$$P_\alpha(E) = \lim_{t \to \infty} |c_{\alpha E}(t)|^2. \qquad (4)$$

The probability distribution $P_\alpha(E)$ can then be computed as

$$P_\alpha(E) = \lim_{t \to \infty} \left| \langle \varphi_{\alpha E} | \mathbb{1} - \Lambda | \Psi(t) \rangle \right|^2. \qquad (5)$$

At first sight, the prescription (5) to extract experimental observables from a wavepacket has the appeal of simplicity since the uncoupled states $\varphi_{\alpha E}$ are usually more easily obtainable than the continuum eigenstates of the full Hamiltonian. This simplicity, though, is misleading since the projector Λ of the total Hamiltonian requires at least a certain number of bound states of the fully interacting system to be known. Since the bound states of H_a are not orthogonal to $\varphi_{\alpha E}$, their elimination is essential. Otherwise they would give rise to spurious contributions to the ionization channels which do not vanish for large times.

A more serious drawback of Eq. 5, however, stems from the imposed asymptotic time limit where the propagation algorithm is limited to $t_{\max}$. Even by the inclusion of part of the long-range interactions between photofragments into the channel Hamiltonian H_0 this problem can only be marginally alleviated rather than solved. More generally, all the methods that require the wavepacket to reach the asymptotic region, i.e. the region where the dynamics governed by H_0 and H_a become equivalent, face the same problem, namely the propagation of the fully correlated wave function for long times and at large distances which may be computationally prohibitively expensive. This limitation becomes particularly severe in a number of circumstances frequently encountered in atomic photoionization. For example, when the wavepacket spectrum is distributed across an ionization threshold, the wavepacket comprises components with vanishingly small kinetic energy that take exceedingly long times to reach the asymptotic region. Even more severe, when several channels with different thresholds are simultaneously open, both slow and fast photoelectrons are present at the same time. Hence, in order for the slowest part of the wave function to reach the asymptotic region, the propagation box must be large enough to accommodate for the fastest components as well. A further difficulty with Eq. 5, perhaps the most relevant in the present context, is provided by resonances in general and by Rydberg series of doubly excited states in particular. First, the convergence of the resonant profiles in those channels where the excited resonances decay requires a propagation time proportional to the lifetime of the longest lived resonance which is excited in the simulation. Second, doubly excited states have, in general, non-vanishing scalar products with all the eigenfunctions of H_0, including those belonging to closed ionization channels.

A.   Projection onto asymptotic channel eigenstates

The simplest and most straightforward implementation of Eq. 5 is to extend the temporal propagation time $t_{\max}$ to the largest value computationally feasible and subsequently project onto (approximate) asymptotic channel eigenstates $\varphi_{\alpha E}$,

$$H_0 | \varphi_{\alpha E} \rangle = E | \varphi_{\alpha E} \rangle. \qquad (6)$$

In the present case of excitation-ionization and double ionization of helium there are two alternative choices for H_0 and $|\varphi_{\alpha E}\rangle$. One choice consists of taking H_0 to be a hydrogenic Hamiltonian with $Z = 1$ for the continuum electron and $Z = 2$ for the bound electron in the case of single ionization, and $Z = 2$ for both electrons in the case of double ionization. Alternatively, asymptotic channel functions are obtained from the diagonalization of the total Hamiltonian in the configuration space where one of the two electrons is frozen in an hydrogenic bound state of the parent ion. These channel functions differ from

the products of Coulomb functions in the radial region where the bound electron density is not zero. The effective potential felt by the free electron deviates from that of a nuclear charge with Z=1. Yet, at larger distances, these channel functions converge to phase-shifted Coulomb functions. Therefore, for the purpose of evaluating the absolute value of the projection of an outgoing wavepacket (Eq. 5), these channel functions and pure Coulomb functions are practically equivalent. As mentioned above, projections onto such asymptotic channel functions at $t_{\max}$ may fail in the presence of long-lived resonances.

B. Projection onto exact scattering states

One avenue to circumvent some of the limitations associated with Eq. 5 is to use, instead of the asymptotic states $\varphi_{\alpha E}$, the exact scattering states $\psi_{\alpha E}^{-}$ of the total atomic Hamiltonian H_a [62]. The $\psi_{\alpha E}^{-}$ states fulfill so-called incoming boundary conditions [63, 64], which are appropriate to the context of photoionization, since photoelectrons are observed in the positive time limit.

Such scattering states satisfy the Lippmann-Schwinger equation with advanced Green's functions [62]

$$\psi_{\alpha E}^{-} = \varphi_{\alpha E} + G_0^{-}(E)H'\psi_{\alpha E}^{-} \quad (7)$$
$$= \varphi_{\alpha E} + G^{-}(E)H'\varphi_{\alpha E} \quad (8)$$

where the operators $G_0^{-}(E) = (E - H_0 - i0^+)^{-1}$ and $G^{-}(E) = (E - H_a - i0^+)^{-1}$ are the resolvents of the channel (H_0) and full Hamiltonian (H_a), while $H' = H_a - H_0$ is the corresponding perturbation (the interactions not accounted for by the channel Hamiltonian H_0).

The $\psi_{\alpha E}^{-}$ states form a complete orthonormal basis for the unbound states of H_a,

$$H_a|\psi_{\alpha E}^{-}\rangle = E|\psi_{\alpha E}^{-}\rangle, \quad \langle\psi_{\alpha E}^{-}|\psi_{\beta E'}^{-}\rangle = \delta_{\alpha\beta}\delta(E - E'), \quad (9)$$

$$\mathbb{1} - \Lambda = \sum_{\alpha} \int d\epsilon\, |\psi_{\alpha\epsilon}^{-}\rangle \langle\psi_{\alpha\epsilon}^{-}|. \quad (10)$$

We can thus write the scattering component $\Psi'(t)$ of the wavepacket at any time t after the external field is over as

$$|\Psi'(t)\rangle = e^{-iH_a(t-t_{\max})}(\mathbb{1} - \Lambda)|\Psi(t_{\max})\rangle =$$
$$= \sum_{\alpha} \int d\epsilon\, |\psi_{\alpha\epsilon}^{-}\rangle\, e^{-i\epsilon(t-t_{\max})}\, c_{\alpha\epsilon}^{-}(t_{\max}) \quad (11)$$

where

$$c_{\alpha E}^{-}(t_{\max}) = \langle\psi_{\alpha E}^{-}|\Psi'(t_{\max})\rangle. \quad (12)$$

A crucial aspect of Eq. 11 is that, in the large time limit, the states $\psi_{\alpha\epsilon}^{-}$ can be replaced by their asymptotes $\varphi_{\alpha\epsilon}$ [63, 64]. This is one defining feature of the $\psi_{\alpha\epsilon}^{-}$

states, sometimes referred to as control of $\psi_{\alpha\epsilon}^{-}$ by the future. In particular,

$$\lim_{t\to\infty} |c_{\alpha E}(t)| = |c_{\alpha E}^{-}(t_{\max})| \quad (13)$$

To compute the distribution $P_\alpha(E)$ we now combine Eq. 4, Eq. 13, and Eq. 12 and obtain the *exact* result

$$P_\alpha(E) = \left|\langle\psi_{\alpha E}^{-}|\Psi(t_{\max})\rangle\right|^2. \quad (14)$$

In contrast to Eq. 5, Eq. 14 requires neither a projection onto the bound states of the system, to which the scattering states are orthogonal, nor the evaluation of a long-time limit. The convenience of using scattering states $\psi_{\alpha E}^{-}$, instead of the asymptotic limits $\varphi_{\alpha E}$, is thus apparent: Eq. 14 can be evaluated as soon as the external time-dependent field is over, without having to wait until the ionizing wavepacket reaches the asymptotic region (Eq. 5).

For single-ionization processes the calculation of scattering states is straightforward. This task has been tackled successfully in the course of the last four decades [65–69]. Today several efficient methods capable of computing multi-electron single ionization scattering states are available. They include the R-matrix [70], J-matrix [71], K-matrix [72, 73], Feshbach projection [74], and inverse iteration [75]. Furthermore, the computational overhead for generating scattering states is easily compensated whenever a large number of different simulations must be carried out, as is the case, e.g., of time-delay scans in pump-probe schemes. Some of the details of our implementation for helium are given in appendix A. The biggest drawback of these methods is that they only work for total energies below the double ionization threshold as no systematic procedure to generate accurate scattering states for double ionization is known to date.

C. Berkeley-ECS method

A third elegant strategy for computing $P_\alpha(E)$, based on exterior complex scaling, was put forward by Palacios, McCurdy and Rescigno [33, 42–44]. In this approach, referred to in this work as the Berkeley-ECS method, the monochromatic component $\Psi_{\mathrm{sc}}(E)$ at energy E of the wavepacket $\Psi(t_{\max})$ is extracted by applying to $\Psi(t_{\max})$ the retarded resolvent $G^+(E)$ of the total Hamiltonian

$$|\Psi_{\mathrm{sc}}(E)\rangle = G^+(E)|\Psi(t_{\max})\rangle. \quad (15)$$

the realization of which in a finite radial domain is provided by the resolvent of an exterior-complex-scaled Hamiltonian H_θ. The scattered wave $\Psi_{\mathrm{sc}}(E)$ is equivalent to the Fourier transform of the time-dependent wavepacket from $t = t_{\max}$ to $t = \infty$. From the function $\Psi_{\mathrm{sc}}(E)$ the distribution of the photofragments is extracted in the asymptotic region. As the wavepacket at the end of the pulse is a square-integrable function, the

asymptotic behavior of the scattered wave can be deduced from the asymptotic form of the Green's function.

Our implementation of the Berkeley-ECS method closely follows that of Palacios *et al.* [33, 43, 44], which builds on earlier work reviewed in [42]. We give a brief overview here and refer the reader to the original papers for details. The central idea is to solve the inhomogeneous linear system (equivalent to Eq. 15),

$$(E - H_a)|\Psi_{\mathrm{sc}}(E)\rangle = |\Psi(t_{\max})\rangle, \qquad (16)$$

in the basis used for temporal propagation (in our implementation using the PETSc package [76]). Purely outgoing boundary conditions are enforced by an exterior complex scaling (ECS) transformation for each of the radial coordinates. Once the scattered wave is obtained, the amplitude $c_{\alpha E}(t_{\max})$ for single ionization can be expressed as [42],

$$c_{\alpha E}(t_{\max}) = \langle \varphi_{\alpha E}|E - H_0|\Psi_{\mathrm{sc}}(E)\rangle, \qquad (17)$$

where $\varphi_{\alpha E}$ is an asymptote of the channel Hamiltonian H_0. The latter should contain the monopolar long-range interaction between the fragments to suppress spurious contributions. Using Green's theorem allows one to express the single ionization amplitude as a surface integral in the non-scaled region of space,

$$c_{\alpha E}(t_{\max}) = \frac{1}{2} \int_S (\varphi_{\alpha E}\boldsymbol{\nabla}\Psi_{\mathrm{sc}}(E) - \Psi_{\mathrm{sc}}(E)\boldsymbol{\nabla}\varphi_{\alpha E}) \cdot \mathrm{d}\mathbf{S}, \qquad (18)$$

where $\boldsymbol{\nabla} = (\nabla_1, \nabla_2)$ is the six-dimensional gradient operator (in the present case of helium). Since the integral (Eq. 18) is evaluated in a radial region far from the atom and $\Psi_{\mathrm{sc}}(E)$ is an outgoing wavepacket by construction, it is sufficient that $\varphi_{\alpha E}$ satisfies the same outgoing boundary conditions as the eigenstates of H_0. Thus, in single ionization, $\varphi_{\alpha E}$ can be taken as the symmetrized product of an ionic bound state and a Coulomb wave with $Z = 1$. For double ionization, a similar expression can be found [42, 43].
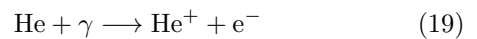
D. Range of applicability

The accuracy of the three extraction methods strongly varies in different spectral regimes. As will be illustrated in more detail below in connection with applications of current interest, the range of applicability can be summarized as follows (Fig. 1).

The projection onto asymptotic channel functions discussed in section III A works well when the wavepacket only contains electrons that are already well-separated in coordinate space. While this is relatively straightforward to achieve at high energies (such as above the double ionization continuum), it becomes prohibitive close to the doubly excited resonances which, for helium, are located in the energy interval from around -0.7 a.u. to 0 a.u., and decay only after many femtoseconds. The main advantages of this approach are its analytical and numerical
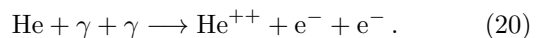
simplicity. For double ionization, the asymptotic channel functions are Coulomb functions with $Z = 2$ and the method can be applied even for long driving pulses when large computational boxes are employed. In the case of single ionization, either hydrogenic channel functions with $Z = 1$ (continuum) and $Z = 2$ (bound state) or the closely related eigenstates obtained by freezing the inner electron in the ionic state can be used. Projection on scattering states (PSS, section III B) works for any separation of the ionized electron from the core, and thus can be used also when doubly excited resonances are excited and before they have decayed. Fully differential photoelectron spectra can be extracted from the wavepacket arising in photoionization by means of a simple projection. However, scattering states are not available above the double ionization threshold as the boundary conditions for double ionization [77] cannot be easily enforced due to the infinite set of constraints they entail (as opposed to the finite number of constraints of single ionization problems). In addition, the scattering states become exceedingly expensive to calculate as the double ionization threshold is approached from below due to the presence of many double Rydberg series. Finally, the Berkeley-ECS method is applicable for both single and double ionization, and also works when resonances and other long-lived states are involved. Its main drawback is the computational complexity: for each desired final energy, a large linear system representing the exterior-complex-scaled Hamiltonian acting on the final wavepacket has to be iteratively solved (Eq. 16). This approach becomes computationally expensive when the system has large spatial extent and when the wavepacket to be analyzed covers a wide range of energies. With currently available supercomputers, this becomes impractical for linear systems with a dimension of more than a few million. For typical simulations in helium this limits the box sizes to the range of $\sim r_{\max} = 250$ a.u. and thus to simulations where only relatively short pulses are used.

IV. APPLICATIONS

We present in this section three benchmark applications for the extraction of scattering information from the wavepacket formation and propagation generated by the interaction of helium with an attosecond XUV pulse absorbing either one photon

$$\mathrm{He} + \gamma \longrightarrow \mathrm{He}^+ + \mathrm{e}^- \qquad (19)$$

or two photons

$$\mathrm{He} + \gamma + \gamma \longrightarrow \mathrm{He}^{++} + \mathrm{e}^- + \mathrm{e}^-. \qquad (20)$$

Helium is the simplest system that features autoionizing states, excited-threshold openings, and a double ionization continuum. Hence the differences between the various methods to extract asymptotic observables from

an ionization wavepacket are particularly transparent in this case. Moreover, a comparison with experimental data and other calculations is possible in some cases. We have carried out two separate simulations, one starting from the ground state 1^1S $(1s^2)$ and one starting from the 2^1S $(1s2s)$ metastable state (lifetime 19.7 ms [78]) of the atom. A short (T_{FWHM}=200 as), moderately intense ($I_{peak} = 10^{12}$ W/cm^2) Gaussian XUV pulse with carrier frequency $\omega = 2.4$ a.u. and $\omega = 1.65$ a.u., respectively, was employed. This Fourier-limited broadband excitation pulse gives access to a large number of doubly excited $^1P^o$ resonances. Moreover, for two-photon absorption, the ^1S and ^1D double ionization continuum is accessed. It also allows for monitoring of time-resolved photoexcitation and ionization near Fano resonances in a pump-probe setting.

A. Photoionization spectrum below the double ionization threshold

The broad spectral width of the attosecond pulse

$$F_{XUV}(t) = \int_0^\infty d\omega \left(\tilde{F}_{XUV}(\omega)e^{-i\omega t} + \text{c.c.} \right) \qquad (21)$$

covers many resonances in the single ionization continuum. For low pulse intensities, where depletion and multi-photon processes can be neglected, it is therefore possible to extract the partial photoionization cross sections σ_α and the dipole anisotropy parameters β_α directly from the partial differential emission probabilities $P_{\alpha E}$ and amplitudes $c_{\alpha E \ell_E}$,

$$\sigma_\alpha(\omega) = \frac{\omega P_{\alpha E}}{j(\omega)}, \qquad (22)$$

with

$$P_{\alpha E} = \sum_{\ell_E} |c_{\alpha E \ell_E}|^2 , \qquad (23)$$

and $E = E_i + \omega$. The index α here characterizes only the remaining quantum numbers of the ionic state while the angular momentum of the continuum electron is now explicitly denoted by ℓ_E. In Eq. 22 $j(\omega)$ is the current density of photons in the pulse with energy ω, $j(\omega) = |\tilde{F}_{XUV}(\omega)|^2 c$. The emission probability $P_{\alpha E}$ is related to the transition matrix element usually employed in the calculation of σ_α through first-order perturbation theory,

$$P_{\alpha E}(\omega) = \left| \int_{-\infty}^\infty dt F_{XUV}(t) e^{i(E-\epsilon_i)t} \langle \varphi_{E\alpha} | z | \varphi_i \rangle \right|^2$$
$$= 4\pi^2 \left| \tilde{F}_{XUV}(\omega = E - \epsilon_i) \right|^2 |\langle \varphi_{E\alpha} | z | \varphi_i \rangle|^2 , \quad (24)$$

with $z = z_1 + z_2$. The anisotropy parameters can be expressed by

$$\beta_\alpha(\omega) = \sqrt{6} \sum_{\ell_E \ell'_E} \Pi_{\ell_E \ell'_E} C^{2\,0}_{\ell_E 0, \ell'_E 0} (-1)^{\ell_E} \begin{Bmatrix} \ell_E & \ell'_E & 2 \\ 1 & 1 & \ell \end{Bmatrix} \times$$
$$\times \frac{c_{\alpha E \ell_E} c^*_{\alpha E \ell'_E}}{P_{\alpha E}} , \qquad (25)$$

where $\Pi_{ab} = \sqrt{(2a+1)(2b+1)}$, $C^{LM}_{\ell_1 m_1, \ell_2 m_2}$ is a Clebsch-Gordan coefficient, and the curly brackets denote a Wigner 6j-symbol. Equation 25 applies to initial states with zero angular momentum and absorption of a single linearly polarized photon. In the present context, the attosecond duration of the XUV pulse permits to compute $\sigma_\alpha(\omega)$ and $\beta_\alpha(\omega)$ in an energy range spanning tens of electronvolts. The three methods described in Sec. III differ in the extraction methods for the amplitudes $c_{\alpha E \ell_E}$ (see Eq. 3 for projection onto Coulomb states, Eq. 12 for the PSS method, and Eq. 18 for the Berkely-ECS method).

A resulting typical photoelectron spectrum as extracted by the three different methods outlined in Sec. III is shown in Fig. 2. While the projection onto asymptotic channel functions can reproduce the smooth background spectrum associated with the direct ionization component very well, it fails to reproduce the sharp structures associated with the autoionizing resonances (see Fig. 1). The spectra calculated with the PSS and with the Berkeley-ECS method feature accurately a large number of resonant profiles and are to within the graphical resolution in excellent agreement with each other. In the following discussion of this subsection, we focus now on the latter two methods. We emphasize that the smaller number of resonances appearing in the Berkeley-ECS method is not due to any fundamental limitation of the method but because of the use of a coarser energy grid. Additional insights can be gained from a close-up (Fig. 3a) and a logarithmic presentation of the photoionization probability (Fig. 3b). Fig. 3 highlights two aspects of the performance of the three methods. First, the projection on scattering states and the Berkeley-ECS method are in excellent agreement close to the resonance (Fig. 3a) and down to the smallest probability densities (Fig. 3b). The deviation of the background profile of the spectrum from a parabola on a logarithmic scale at low energies is due to the fact that the Gaussian envelope of the XUV pulse is eventually truncated. Second, the spectrum obtained through the projection on Coulomb functions clearly deviates from the background below -1 a.u., however, only when $P(E)$ is already small ($\lesssim 10^{-4}$ of the direct ionization peak). This error due to the contamination by doubly excited states is small in the present case since they provide only a minor admixture to the wavepacket. When they have a higher relative weight, however, their spurious effect on the spectrum can be larger. The convergence of the DES spectrum as a function of the size of the close-coupling expansion within the PSS is illustrated in Fig. 4. Here, the PSS employs a minimal close-coupling expansion involving the open

channels ($1s\epsilon_p$, $2s\epsilon_p$, $2p\epsilon_s$, and $2p\epsilon_d$) only. Clearly, since the $N = 3$ channels (those corresponding to the He$^+$ parent ion in the $3s$, $3p$, and $3d$ states) are not included, the higher members of the autoionizing Rydberg series converging to the N=3 threshold are not reproduced. As a consequence, the spectrum obtained with the PSS deviates from the one obtained with the Berkeley-ECS method at energies higher than -0.3 a.u. . On the other hand, the spectrum below the $N = 3$ threshold is already well converged, i.e. the influence of the closed channels is adequately accounted for. This observation highlights the salient feature of the close-coupling expansion with pseudostates, namely the possibility to drastically truncate the representation while still obtaining an accurate representation of the continuum states in a given single-ionization energy region. Having established the convergence, accuracy, and excellent agreement of the PSS and the Berkeley-ECS methods for single ionization spectra below the double ionization (Fig. 1), we turn now to a comparison with available experimental data and calculations for the $N = 2$ photoionization cross section $\sigma_2(\omega)$ (Eq. 22) and anisotropy parameter $\beta_2(\omega)$ (Eq. 25). For photoexcitation of the He($1s^2$) ground state, several experimental datasets for $\sigma_2(\omega)$ and $\beta_2(\omega)$ measured with synchrotron radiation are available (Fig. 5). Moreover, this process has served over the years to benchmark theoretical descriptions of photoemission in a strongly correlated system (see, e.g., [79–82] and references therein). For clarity, we display in Fig. 5 only a small selection of theoretical datasets. While for cross sections (Fig. 5a) several experimental datasets as well as theoretical results are in close agreement with each other, there are still unresolved discrepancies for the β_2 parameters (Fig. 5b). Increased sensitivity of β_2 to the approximations employed is not surprising as, unlike energy distributions, angular distributions depend on the relative phases between photoionization amplitudes in different channels as well as on their absolute values. Earlier results by Sanchez and Martín [84] lie closer to the experimental data by Menzel et al. [85]. By contrast, the more recent calculation by Moccia and Spizzo [68] agrees significantly better with the data by Lindle et al. [87]. The present two complementary methods (PSS, Berkeley-ECS) agree, within the graphical resolution, perfectly with each other and with the calculation of Moccia and Spizzo [68] and also of Venuti et al. [88]. Thus, it appears that the measurements of the β_2 parameter by Lindle et al. between the $N = 2$ and $N = 3$ thresholds are consistent with theory. We note that our theory curves in Fig. 5 pertain to perfect spectral resolution while the experimental spectral resolution in the experiment of Lindle et al. [87] was $\Delta E \approx 170$meV due to monochromator broadening. Folding our $\beta_2(\omega)$ with the experimental resolution would further improve the agreement near sharp resonances.

Unlike excitation from the ground state, the excitation of doubly excited resonances starting from the metastable ^{1}S ($1s2s$) state is still an experimental challenge due to the difficulty of producing a sample with the required optical thickness. Theoretical treatments of this process have also been scarce [89–91]. First experimental results for some doubly excited states below the N=2 threshold only became available recently [92]. Our present simulation of the excitation by an XUV pulse with central frequency $\omega = 1.65$ a.u. appears to be the first that provides information on the β_2 parameter (Fig. 6). The results from the PSS and Berkeley-ECS method agree to within the graphical resolution. It is now of interest to compare the excitation spectrum and β_2 parameters for the same final energies when accessed from different initial states. This allows to probe propensity rules for radiative and non-radiative transitions between strongly correlated excited states [79]. As a prototypical example we focus in the following on the spectrum in the proximity of the first ^{1}P^o autoionizing resonance below the $N = 3$ threshold, i.e., reached for photon energies between 68 eV and 71 eV starting from the ground state, and for photon energies between 47.5 eV and 50.5 eV starting from the metastable He($1s2s$) state (Fig. 7).

For resonances of doubly excited states several equivalent classification schemes signifying the departure from the independent particle model are in use [80, 93–97]. We employ in the following the so-called parabolic classification scheme within which each resonance of a given symmetry $^{2S+1}L^\pi$ is uniquely identified by the notation $[N_1 N_2 m]_n^A$, where N_1, N_2 and m are the Stark quantum numbers in parabolic coordinates for a hydrogenic ion in an external uniform electric field, $A = \pm 1$ indicates whether the wave function has an anti-node ($+$) or a node ($-$) when the two electrons are at the same distance from the nucleus, $r_1 = r_2$, and n is the principal quantum number of the outer electron. The corresponding continuum scattering channels above the $N = N_1 + N_2 + m + 1$ threshold are labeled by $[N_1 N_2 m]^A$ (i.e., with the n index dropped). The parabolic classification scheme is particularly well suited to formulate propensity rules, i.e., dominant channels in branching ratios. The resonance investigated in Fig. 7 carries the parabolic label $[011]_3^+$. According to autoionization propensity rules, the $[011]_n^+$ series autoionizes to the $[001]^+$ continuum through the efficient configuration interaction coupling ($[011]_n^+ \leftrightarrow [001]^+$) characterized by $\Delta N_2 = -1$. Indeed, the lifetime of the $[011]_3^+$ resonance is short, $\tau = 3.44$ fs, highlighting the efficient coupling. The autoionizing branching ratios for decay of this resonance are $b_{1s\epsilon_p} = 0.019$ (corresponding to the $[000]^-$ channel in the parabolic classification), and $b_{2s\epsilon_p} = 0.141$, $b_{2p\epsilon_d} = 0.308$, and $b_{2p\epsilon_s} = 0.532$ [68], the latter corresponding to the $[001]^+$ channel. Photoexcitation of the $[011]_3^+$ resonance from the symmetric ground state (i.e., with two equivalent electrons) follows similar propensity rules for radiative transitions [79] which, in this case, predict that the transition is very weak. Clearly, the dominant excitation channel $1s\epsilon p$ corresponding to $[000]^-$, present already at the independent particle level, does not directly couple to autoionizing resonances. The subdominant channel $[001]^+$ couples to the resonance $[011]^+$ via configuration interaction, as dis-

cussed above. Consequently, all partial cross sections σ_α ($\alpha = 2\ell, E\ell_E$) should resemble the Fano model for an isolated resonance with energy E_r and width Γ_r embedded in a single-channel continuum [98], namely,

$$\sigma_\alpha(E) = \sigma_{bg}(E) b_\alpha \frac{(\epsilon + q)^2}{\epsilon^2 + 1}, \quad \epsilon \equiv 2(E - E_r)/\Gamma_r \quad (26)$$

where $\sigma_{bg}(E)$ is a smooth background total cross sections and q is the Fano asymmetry parameter. The quantity $\pi q^2/2$ expresses the ratio between the probability to excite the resonance and that of exciting the continuum in an energy interval equal to the resonance width. Therefore, in this case, we expect a very small asymmetry parameter q giving rise to a typical window resonance shape. In particular, *all the partial cross sections should vanish, or almost vanish, at the same energy close to the resonance position* (Fig. 7c). In turn, the β_2 parameter is expected to closely follow that for the $[001]^+$ channel, $\beta_2 \approx 0$, far from the resonance as, indeed, observed (Fig. 7b). Close to the resonance, however, a sharp peak in β_2 is observed. The origin of this modulation of β_2 follows directly from the variation of the partial cross section (Fig. 7c). Even though all $N = 2$ partial cross sections approach values near zero at around $E = 69.8$ eV, the $2s\epsilon_p$ cross section misses the zero by a small yet significantly larger amount than the other two channels. As a result, close to the resonance, the relative proportion of the channels changes abruptly. At the minimum of the $N = 2$ cross section, the $2s\epsilon_p$ channel ($\beta_2 = 2$) dominates and the β_2 parameter has a sharp maximum close to the theoretical limit 2. As soon as the Fano minimum is passed, the asymmetry parameter drops back to zero again. Therefore, the sharp modulation in the β_2 parameter for $N = 2$ for excitation from the ground state is a dramatic magnification of the *slight* misalignment between the $N = 2$ decay channel of the $[011]_3^+$ resonance and the $N = 2$ dipole excitation channel giving rise to a local break-down of the propensity rules. A significantly different scenario applies to photoexcitation from the $(1s2s)$ state. Since the initial state features inequivalent electrons, the initial state qualifies as non-symmetric within the framework of propensity rules. Therefore, the propensity rule derived by the saddle-point approximation [79] no longer applies. Yet, even simpler rules apply here: both the $1s2s \to 1s\epsilon_p$ and $1s2s \to 2s\epsilon_p$ transitions are allowed already at the level of the independent particle approximation resulting in a 50 fold increased cross section (see Figs. 7ac). As a consequence, the background β_2 parameter is expected to be very close to 2 (Fig. 7b). Moreover, the direct transition to the $[011]^+$ channel is allowed resulting in a remarkably large q parameter $\simeq -4.6$ [89] and an almost Lorentzian resonance profile (Fig. 7a). Consequently, near the resonance the β_2 value drops locally to values associated with the $[001]^+$ channel, i.e., $\beta_2 \approx 0$ (Fig. 6b). Experimental verifications of these predictions would provide sensitive tests for the applicability of propensity rules and would be of considerable interest.

B. Time-resolved autoionization resonances in helium

With the availability of attosecond XUV pulses with durations small compared to the lifetime of the resonances, the time-evolution of the excitation and decay of an autoionizing resonance can be monitored in real time. The two-path interference between the direct ionization (e.g. the $[001]^+$ channel) and the indirect ionization via quasi-bound states (the $[011]_3^+$ states in the example of the previous subsection) gives rise to non-stationary coherent dynamics in the continuum. Quantitative features of the temporal evolution have been predicted for a generic Fano resonance model [99–101]. With the present accurate wavepacket propagation and extraction protocol, it will be possible for the first time to monitor with unprecedented resolution the evolution of single-ionization resonant profiles for helium in a pump-probe setting employing ultrashort and intense light pulses. Here, the doubly excited states are populated in the initial (pumping) step and the double ionization continuum is accessed in the final (probing) step.

Monitoring the time evolution of the continuum portion of the wavepacket generated by the XUV attosecond pulse (see Eq. 4)

$$P_\alpha(E, t) = |c_{\alpha E}(t)|^2 \quad (27)$$

necessarily requires projection at finite times, i.e., in the non-asymptotic region where the asymptotic channel Hamiltonian does not yet apply. Therefore, the observables associated to the time-resolved quantity $P_\alpha(E, t)$ must be obtained through an additional interrogation step akin to a pump-probe setting. In the previous analysis of time-resolved Fano resonances, attosecond streaking employing an additional few-cycle IR pulse was proposed for the interrogation (probing) step [99–101]. Below, we propose an alternative XUV-XUV pump-probe sequence (see Eq. 20) bearing resemblance to the attosecond transient absorption (ATA) protocol [37].

It is now instructive to analyze Eq. 27 for the wavepacket simulated by projecting at finite times onto the channel eigenstates (see section III A), either onto symmetrized products of a bound ($Z = 2$) and a continuum ($Z = 1$) Coulomb function (Fig. 8), or alternatively, projecting onto partial-wave channel functions with a frozen core (see section III A). Both lead to an almost identical quantum beat pattern lending credence to the physical significance of the ensuing interference fringes. The build-up and decay of the dominant series sp_n^+ of $^1P^o$ autoionizing resonances corresponding to the series $[001]^+$ in the parabolic classification scheme is clearly visible (Fig. 8a). This time-dependent spectrum $P(E, t)$ extracted from the ab-initio simulation can be directly compared with the analytic prediction for the time evolution of generic Fano resonances. Wickenhauser *et al.* derived a closed expression $P(E, t)$ for an isolated resonance in the impulsive (i.e., broad-band excitation)

limit [99, 101],

$$P(E,t) \propto P_{E0} \left| 1 + (i-q)\frac{\Gamma}{2} \frac{e^{-i(\tilde{E}_a - E)t} - 1}{E - \tilde{E}_a} \right|^2, \quad (28)$$

where P_{E0} is the dipole transition strength between the initial ground state and the unperturbed continuum, q is the Fano asymmetry parameter [98], Γ is the resonance width and $\tilde{E}_a = \tilde{E}_a^{\Re e} - i\Gamma/2$ is the complex energy of the resonance. This expression can be easily extended to the case of many isolated resonances on top of a smooth background

$$P(E,t) \propto P_{E0} \left| 1 + \sum_j (i-q_j)\frac{\Gamma_j}{2} \frac{e^{-i(\tilde{E}_j - E)t} - 1}{E - \tilde{E}_j} \right|^2.$$
$$(29)$$

We apply Eq. 29 by including the first nine terms ($n = 2, 3, \cdots, 10$) of the sp^+ $^1P^o$ series. The positions E_n, widths Γ_n, and asymmetry parameters q_n of the nth term are approximated by $E_n = E_{N=2} - 1/2(n-\mu)^2$, $\Gamma_n = \bar{\Gamma}/(n-\mu)^3$, and $q_n = q$, where μ, $\bar{\Gamma}$, and q are the quantum defect, the reduced width and the asymmetry parameter of the series, thereby extrapolating the approximate values $\mu = 0.3$, $\bar{\Gamma} = 0.007$, $q = -2.6$ taken from accurate calculations for the low members of the series available in the literature [79]. The spectrum is multiplied by a Gaussian envelope $\exp(-\frac{1}{2}((E-E_0)/\sigma)^2)$ with $\sigma = 0.127$ to reproduce the Fourier-width of an attosecond pulse. This correction to the impulsive limit is justified as long as the duration of the pulse is much smaller than the lifetime of all resonances involved. The resulting agreement between the analytic model (Eq. 29, Fig. 8a) and the ab-initio wavepacket simulation (Fig. 8b) is remarkable: all features of the interference fringes associated with different resonances are qualitatively and, to a good degree of approximation, even quantitatively reproduced. The details of the temporal interference fringes present in the wavepacket simulation are highlighted in the close-up of the spectrum near the sp_2^+ $^1P^o$ (or $2s2p$ or $[001]_2^+$) resonance (Fig. 9). For small times, the photoelectron spectrum rapidly builds-up from zero to a smooth Gaussian profile mirroring the temporal evolution of the attosecond pulse. At this stage, only the "direct ionization" component is visible since the duration of the pulse is much shorter than the lifetime of the resonance. With increasing time, hyperbolic-shaped interference fringes in the $E - t$ plane converging towards the resonance appear on both flanks. They have been first observed for the generic time-dependent Fano-resonance model [99–101] but appear in the ab-initio simulation as well. These quantum beats follow directly from Eq. 28. The ridges (valleys) are given by the condition $(E_a - E)t = n\pi$. Appearance of this quantum beat structures in the continuum is not limited to Fano resonances but is universal whenever the continuum is accessed both directly and via a (quasi) bound state. More recently, similar structures were found in

attosecond XUV-IR pump-probe electron interferometry for continuum electrons just above the first ionization threshold [102]. Finally, for $t \to \infty$ the stationary Fano-resonance profile emerges. The point to be noted is that this asymptotic profile shown in Fig. 9 is determined by the PSS method by projecting the wavepacket onto exact scattering states ψ_{1sE}^- (Eq. 14) right after the conclusion of the pulse, i.e., during the early stages of the evolution depicted in Fig. 9. The scattering states implicitly account for the time evolution of the full wavepacket to infinity and no free propagation beyond the end of the pulse is required. In turn, quantum beats observable at finite time are not visible in the PSS method as it projects into the asymptotic future. The experimental observation of the temporal interference pattern requires an interrogation of the system at finite times, i.e., before the asymptotic scattering regime is reached, e.g. by IR streaking [99–101]. As an alternative to streaking we propose here to employ a time-delayed XUV pulse that probes the quasi-bound rather than the continuum component of the Fano resonance. In such an XUV-XUV pump-probe setting the population of the localized component is suddenly depleted by the second attosecond pulse. In close analogy to the analytic model for projective interrogation of the continuum (Eq. 28), we find for the asymptotic energy distribution of the continuum electron as a function of the delay time τ at which the quasi-bound state is impulsively removed

$$\bar{P}(E,\tau) \propto |P_{E0}|^2 \left| +(i-q)\frac{\Gamma}{2} \frac{e^{-i(\tilde{E}_a - E)\tau} - e^{2i\varphi_q}}{E - \tilde{E}_a^*} \right|^2,$$
$$(30)$$

where $\varphi_q = \arctan(q)$. This protocol resembles the attosecond transient absorption employed to time-resolve core-level dynamics [37]. In fact, Pfeifer and co-workers [103] recently implemented the attosecond transient absorption analogue of this experimental scheme and, indeed, interference fringes similar to those described here were observed and theoretically confirmed by one of us with full *ab-initio* simulations [104]. It is now of interest to quantitatively compare the two interrogation protocols (Eq. 28 and Eq. 30) displayed in Fig. 10. Projection onto the continuum portion (Fig. 10a) and the complementary operation of projecting out the bound portion (Fig. 10b) yields nearly identical quantum beat patterns for a series of autoionizing resonances. The difference between the two (Fig. 10c) is remarkably small. This result suggests the direct experimental observability of the temporal interference fringes by the XUV-XUV pump-probe scheme.

C. Two-photon double ionization

We turn now to the process of probing the two-electron continuum portion of the wavepacket (Eq. 20). We analyze the correlated wavepacket for the doubly ionized part of the spectrum caused by two-photon absorp-

tion of the previously used Gaussian XUV pulse with $T_{\text{FWHM}}=200$ as and a carrier frequency $\omega = 2.4$ a.u. from the helium ground state. In this regime, the PSS is not applicable because of the lack of accurate scattering states for the double continuum. However, the Berkeley-ECS method (see section III C) is able to impose the correct boundary conditions and obtain the asymptotic spectral information of a doubly ionized wavepacket directly after the completion of the laser pulse. The projection of the wavepacket on an uncorrelated, symmetrized product of two Coulomb functions with $Z = 2$ is straightforward (see section III A). However, it requires the propagation of the wavepacket to large distances in order to control and minimize the error due to the neglect of the electron-electron interaction. In practice this yields accurate results as long as the box and angular momentum basis are large enough to correctly represent the wave function at the time of projection. We first compare the singly differential photoelectron spectrum with the prominent two peaks near the expected positions for the sequential two-photon double ionization process corresponding to the emission of the "first" electron (Eq. 19) with a kinetic energy of $E_1 = \omega - I_{p,1} \approx 1.5$ a.u. (I_p: ionization potential) and the subsequent emission of the second electron with $E_2 = \omega - I_{p,2} \approx 0.4$ a.u., Fig. 11. Note that the separation between the two maxima is smaller than predicted by the sequential limit due to the energy exchange between the two electrons enforced by strong temporal correlation between the two emission events. In the present case, it is not the carrier frequency $\omega > 2$ a.u. which lies above the threshold for non-sequential ionization but the short pulse duration that controls the degree of non-sequentiality of the emission process. The projection onto Coulomb waves 7 fs after the peak of the pulse shows excellent agreement with the spectrum obtained by the Berkeley-ECS method using the wavepacket immediately after the conclusion of the pulse (Fig. 11). In fact, virtually the same level of agreement is already reached for considerably smaller propagation times before the projection (not shown). Even projection directly after the conclusion of the field (1 fs after the peak of the XUV pulse, red line in Fig. 11) gives very similar results.

The fact that the pulse duration has a profound effect on the two-photon two-electron emission process that goes beyond a Fourier broadening [52, 105] becomes more apparent when one studies the angular correlation between the photofragments [13, 44, 106, 107]. For example the energy-integrated conditional angular emission probability for one electron when the other electron is ejected along the laser polarization axis (Fig. 12a) displays pronounced deviations from a simple dipolar pattern expected for sequential double ionization. Such structures have been previously observed both by projecting on Coulomb waves [13] and with the Berkeley-ECS method [44]. We find excellent agreement between the two methods within the graphical resolution of Fig. 12a. The remaining small residual differences between the two methods can be understood by inspect-

ing their respective convergence behavior: the projection onto Coulomb functions becomes more accurate when the electrons have spread further apart before the spectral analysis is performed, provided the partial wave expansion of the wave function covers enough angular momenta to accurately describe the motion of the free electrons. For the present case convergence is reached for propagation times of about 7 fs after the peak of the XUV pulse (see the solid lines in Fig. 12b). For the Berkeley-ECS method the extension of the computational box for the transformation to the spectral domain (i.e. the solution of Eq. 16) and for the surface integral (cf. Eq. 18) influences the quality of the results. Thus, for accurate angular distributions comparably large radial boxes are also required for the Berkeley-ECS method (see the dotted lines in Fig. 12b). The convergence behavior of the two methods is linked: their results for the angular distributions agree when the extraction radius of the Berkeley-ECS method roughly equals the position (of the relevant parts) of the wavepacket at the time of projection on the Coulomb functions (compare solid and dotted lines in Fig. 12b). Thus, for larger ECS boxes even the small differences to the (converged) Coulomb projection in Fig. 12a would vanish. For both methods the convergence for the angular distributions is considerably slower than for the energy spectra, especially where both electrons are emitted in the same direction (Fig. 12b). The latter highlights the fact that those regions in phase space where electron-electron correlation is strongest still pose a major challenge for highly accurate ab-initio simulations. Since this region of mutual repulsion contributes, however, little to total emission probabilities, the overall accuracy remains largely unaffected.

V. CONCLUSIONS

We have analyzed and applied three different methods to extract the continuum component of a correlated multi-electron wave function in helium obtained from an ab-initio solution of the time-dependent Schrödinger equation. Each of the three methods investigated, the projection onto asymptotic channel functions, i.e., Coulomb continuum states, the projection onto exact scattering states (PSS), and the Berkeley-ECS method feature both advantages and disadvantages depending on the energy range of interest, the required box size, and whether single or double ionization distributions are desired. Below the double ionization threshold, methods to extract photoelectron spectra that are based on the projection on approximated continuum channels such as Coulomb continuum functions work well when no resonances are significantly populated, but become inapplicable in spectral regions in the vicinity of narrow resonances. In this regime, remarkably good agreement between the PSS and the Berkeley-ECS method is observed. This finding suggests an efficient way of monitoring the composition of a complex wavepacket ψ in the single-

ionization channels below the double ionization threshold. Since the scattering states can be computed separately, once and for all, in an adapted basis, the extraction of the expansion coefficients of ψ requires only the calculation of a simple scalar product. Above the double ionization threshold, the PSS becomes inapplicable while the Berkeley-ECS method agrees well with projection onto Coulomb functions provided the computational box is sufficiently large and the wavepacket is propagated into the asymptotic region. The three applications presented explored different aspects of attosecond-pulse-driven wavepacket dynamics. Exploiting the broad spectral width we presented converged calculations for the photoionization cross section and anisotropy parameter below the double ionization threshold including first results for spectra and angular distributions for photoionization of metastable He($1s2s$, ^{1}S). Comparison to the corresponding ground state process provides insights into the applicability of the propensity rules for excitation and decay of doubly excited resonances. Exploiting the short duration of the pulse we have provided first ab-initio results for time-resolved autoionizing resonances and have suggested a new protocol for observing the ensuing quantum beats complementing attosecond streaking. Furthermore, we have verified that two-electron wavepackets above the double ionization threshold acquire features of non-sequential emission for ultrashort pulses notwithstanding the fact that the mean photon frequency lies well above the threshold where sequential ionization should prevail.

Appendix A: Implementation of the PSS for helium

Accurate scattering states (Eq. 7) and corresponding projection amplitudes (Eq. 12) can be calculated for energies below the double ionization threshold. In the present case, the single-ionization scattering states of helium below the double ionization threshold of the atom are computed with the B-spline K-matrix method. B-splines are a convenient tool to accurately represent the radial component of continuum atomic orbitals on a finite interval [108, 109], while the K-matrix method [72] is an L^2 realization of configuration interaction in the continuum along the lines of Fano's pioneering paper [98]. The K-matrix method has been successfully applied for the single-photoionization spectrum of several atomic and molecular systems [68, 73, 90, 110, 111]. We will provide here only a brief description of its implementation for the case of helium (details can be found elsewhere [73, 112]).

A complete set $\psi_{\alpha E}^{\mathcal{P}}$ of stationary eigenfunctions of the field-free Hamiltonian H_a at a given energy E in the single-ionization continuum are sought in the form of a linear combination of partial-wave channel functions $\phi_{\alpha E}$ (PWC's), plus an additional component from a localized (or pseudostate) channel (LC),

$$\psi_{\alpha E}^{\mathcal{P}} = \phi_{\alpha E} + \sum_{\gamma} \sum\!\!\!\!\!\!\int d\epsilon\, \phi_{\gamma\epsilon} \frac{\mathcal{P}}{E - \epsilon} \mathbf{K}_{\gamma\epsilon,\alpha E}, \qquad (A1)$$

where the index α runs over the channels which are open at energy E, while the index γ runs over all open and closed channels, including the localized one.

The PWC α is defined by coupling and antisymmetrizing a bound state of the He$^+$ parent ion with quantum numbers N_α and L_α and energy E_α, to an electron state with angular momentum ℓ_α, the radial degree of freedom of which is otherwise unconstrained, to give a state with definite values for the total spin S and angular momentum L.

$$\phi_{\alpha E} = \hat{\mathcal{A}}\, \Theta_{S\Sigma}\, \mathcal{Y}_{L_\alpha \ell_\alpha}^{LM}(\Omega_1, \Omega_2)\, R_{N_\alpha L_\alpha}(r_1) \frac{f_{\alpha E}(r_2)}{r_2},$$
$$(A2)$$

where $\hat{\mathcal{A}}$ is the antisymmetrizer, $\Theta_{S\Sigma}$ is a two-electron spin function, $R_{N_\alpha L_\alpha}$ is the radial part of the frozen He$^+$ parent ion state, and $f_{\alpha E}$ the continuum radial function. Asymptotically, the $f_{\alpha E}$ are a linear combination of the regular and irregular Coulomb functions with angular momentum ℓ_α, energy E, and a phase shift $\delta_{\alpha E}$, determined by the short range behavior of the differential equation for $f_{\alpha E}$, which differs from that of the hydrogenic functions. This results from the deviation of the frozen-core potential from that of a pure Coulomb potential.

The PWCs in (Eq. A1) do not exhaust the state space associated with single ionization, because the set of bound states of the parent ion is not complete, and because the close-coupling expansion (Eq. A1) is truncated. Nevertheless, if all single- and double-ionization

closed channels were to be included in the close-coupling expansion, their contribution would decay exponentially at large radii. Therefore, instead of using a complete basis, it is sufficient to include in (Eq. A1) a pseudo-state channel LC that comprises a sufficiently large number of normalized two-electron functions built from localized orbitals, to attain good accuracy.

Equation (A1) may be solved for the unknown coefficient matrix $\mathbf{K}$ by requiring $\psi_{\alpha E}^{\mathcal{P}}$ to be an eigenfunction of the complete projected Hamiltonian with eigenvalue E,

$$\langle \phi_{\beta E'} |\, E - H_a\, | \psi_{\alpha E}^{\mathcal{P}} \rangle = 0 \quad \forall \beta, E'. \qquad (A3)$$

This condition leads to a system of integral equations for $\mathbf{K}$ which can be discretized and solved with standard linear algebra routines. The scattering states with definite spherical symmetry $\psi_{\alpha E}^{-}$ are then computed as

$$\psi_{\alpha E}^{-} = \sum_{\beta} \psi_{\beta E}^{\mathcal{P}} \left[\frac{1}{\mathbf{1} - i\pi\mathbf{K}(E)} \right]_{\beta\alpha} e^{-i(\sigma_{\ell_\alpha} + \delta_\alpha - \ell_\alpha \pi/2)},$$
$$(A4)$$

where $\mathbf{K}_{\alpha\beta}(E) \equiv \mathbf{K}_{\alpha E, \beta E}$ is the on-shell reactance matrix (§7.2.3 in [62]) while σ_{ℓ_α} and δ_α are the Coulomb and channel phase shifts, respectively. Finally, the scattering states which correspond to Coulomb plane waves associated with a parent ion in a given state A, are given by

$$\psi_{A,E\Omega\sigma}^{-} = \sum_{\alpha}^{\substack{L_\alpha = L_A \\ N_\alpha = N_A}} C_{L_A M_A, \ell m}^{LM} C_{\frac{1}{2}\Sigma_A, \frac{1}{2}\sigma}^{S\Sigma} Y_{\ell m}^{*}(\Omega)\ \psi_{\alpha E}^{-}, \quad (A5)$$

where L_A, M_A, and Σ_A indicate the angular momentum and spin of the parent ion, Ω and σ indicate the asymptotic photoelectron's direction and spin, and $C_{a\alpha, b\beta}^{c\gamma}$ are Clebsch-Gordan coefficients. The states $\psi_{A,E\Omega\sigma}^{-}$ are normalized according to

$$\langle \psi_{A,E\Omega\sigma}^{-} | \psi_{B,E'\Omega'\sigma'}^{-} \rangle = \delta_{AB}\delta_{\sigma\sigma'}\delta(E - E')\delta(\Omega - \Omega'). \quad (A6)$$

Appendix B: Conversion of B-spline close-coupling functions to the FEDVR basis

One technical key feature of the present method of projecting onto accurate scattering states (PSS) is that the calculation of scattering states is independent of the actual simulation and can be optimized separately. Yet, scattering states have so far been employed only in those cases where they are built in the same basis which is used to carry out the time-dependent simulations. We demonstrate here that the scattering states computed in an optimized B-spline close-coupling basis with the K-matrix method [73] can be accurately converted to a finite-element discrete-variable (FEDVR) basis [32] optimized for time propagation. Table I compares the energies of $^1\mathrm{S}^e$, $^1\mathrm{P}^o$, and $^1\mathrm{D}^e$ helium Rydberg states with principal

quantum number n for the outer electron up to $n=6$, obtained by diagonalizing the full configuration interaction Hamiltonian of helium built in either the FEDVR or the B-spline basis. The FEDVR basis comprised eleven functions per finite element. The width of the first element was 2 a.u. and increased linearly to 4.0 a.u. within the first 5 finite elements. The grid extensions were 28 a.u. for one radial coordinate and 156 a.u. for the other. The B-spline basis comprised spline functions of order $k = 8$ [108] defined on a non-uniform grid of nodes, optimized at small radii to optimize the representation of the ground state of the helium atom, and with an asymptotic spacing between consecutive nodes of 0.5 a.u. up to a maximum radius of 800 a.u.. For both the FEDVR and the B-spline basis, the maximum orbital angular momentum $\ell_{max} = 4$ (which suffices for the present comparison between methods) was used. The very good agreement between the two approaches for the Rydberg spectrum indicates that the wave functions in the two bases are represented at comparable levels of accuracy. To assess the accuracy with which the wave functions computed in the B-spline basis are converted to the FEDVR basis we computed the norm of the converted Rydberg states $\langle \tilde{\phi}_n | \tilde{\phi}_n \rangle$ as well as their overlap $\langle \phi_n | \tilde{\phi}_n \rangle$ with the corresponding states computed directly in the FEDVR basis. Both numbers should within the numerical accuracy be close to 1. The errors $\tilde{\delta}_n = 1 - \langle \tilde{\phi}_n | \tilde{\phi}_n \rangle$ and $\delta_n = 1 - \langle \phi_n | \tilde{\phi}_n \rangle$ for the states listed in table I are between 10^{-11} and 10^{-7} (table II).

This confirms the accuracy of the conversion from the B-spline to the FEDVR basis. The error is larger for the ground state than for the excited states because the first finite element is still comparatively wide and could be reduced further by choosing a smaller radial span for the first few finite elements.

[1] G. Sansone, L. Poletto, and M. Nisoli, Nature Photonics **5**, 655 (Sep. 2011), ISSN 1749-4885, http://www.nature.com/doifinder/10.1038/nphoton.2011.167.

[2] B. W. J. McNeil and N. R. Thompson, Nature Photonics **4**, 814 (2010).

[3] A. D. Shiner, B. E. Schmidt, C. Trallero-Herrero, H. J. Wörner, S. Patchkovskii, P. B. Corkum, J.-C. Kieffer, F. Légaré, and D. M. Villeneuve, Nature Physics **7**, 464 (2011), ISSN 1745-2473, http://dx.doi.org/10.1038/nphys1940.

[4] M. Schultze, M. Fiess, N. Karpowicz, J. Gagnon, M. Korbman, M. Hofstetter, S. Neppl, A. L. Cavalieri, Y. Komninos, T. Mercouris, C. A. Nicolaides, R. Pazourek, S. Nagele, J. Feist, J. Burgdörfer, A. M. Azzeer, R. Ernstorfer, R. Kienberger, U. Kleineberg, E. Goulielmakis, F. Krausz, and V. S. Yakovlev, Science **328**, 1658 (2010).

[5] O. Smirnova, Y. Mairesse, S. Patchkovskii, N. Dudovich, D. M. Villeneuve, P. B. Corkum, and M. Y. Ivanov, Nature **460**, 972 (Aug. 2009), ISSN 1476-4687, http://www.ncbi.nlm.nih.gov/pubmed/19626004.

[6] S. Haessler, J. Caillat, W. Boutu, C. Giovanetti-Teixeira, T. Ruchon, T. Auguste, Z. Diveki, P. Breger, A. Maquet, B. Carré, R. Taïeb, and P. Salières, Nature Physics **6**, 200 (2010), ISSN 1745-2473, http://dx.doi.org/10.1038/nphys1511.

[7] J. Feist, S. Nagele, C. Ticknor, B. I. Schneider, L. A. Collins, and J. Burgdörfer, Phys. Rev. Lett. **107**, 093005 (2011).

[8] J. Caillat, A. Maquet, S. Haessler, B. Fabre, T. Ruchon, P. Salières, Y. Mairesse, and R. Taïeb, Phys. Rev. Lett. **106**, 093002 (2011).

[9] K. Klünder, J. M. Dahlström, M. Gisselbrecht, T. Fordell, M. Swoboda, D. Guénot, P. Johnsson, J. Caillat, J. Mauritsson, A. Maquet, R. Taïeb, and A. L'Huillier, Phys. Rev. Lett. **106**, 143002 (2011).

[10] A. I. Kuleff and L. S. Cederbaum, Phys. Rev. Lett. **106**, 053001 (Jan. 2011), ISSN 0031-9007, http://link.aps.org/doi/10.1103/PhysRevLett.106.053001.

[11] T. Remetter, P. Johnsson, J. Mauritsson, K. Varjú, F. Lépine, E. Gustafsson, M. F. Kling, J. I. Khan, R. López-Martens, K. J. Schafer, M. J. J. Vrakking, and A. L'Huillier, Nature Physics **2**, 323 (2006).

[12] J. Mauritsson, P. Johnsson, E. Mansten, M. Swoboda, T. Ruchon, A. L'Huillier, and K. J. Schafer, Phys. Rev. Lett. **100**, 073003 (2008).

[13] J. Feist, S. Nagele, R. Pazourek, E. Persson, B. I. Schneider, L. A. Collins, and J. Burgdörfer, Phys. Rev. Lett. **103**, 063002 (Aug. 2009).

[14] L. Argenti and E. Lindroth, Phys. Rev. Lett. **105**, 053002 (Jul. 2010), ISSN 0031-9007, http://link.aps.org/doi/10.1103/PhysRevLett.105.053002.

[15] G. Sansone, F. Kelkensberg, J. F. Pérez-Torres, F. Morales, M. F. Kling, W. Siu, O. Ghafur, P. Johnsson, M. Swoboda, E. Benedetti, F. Ferrari, F. Lépine, J. L. Sanz-Vicario, S. Zherebtsov, I. Znakovskaya, A. L'Huillier, M. Y. Ivanov, M. Nisoli, F. Martín, and M. J. J. Vrakking, Nature **465**, 763 (Jun. 2010), ISSN 0028-0836, http://www.nature.com/doifinder/10.1038/nature09084.

[16] F. Kelkensberg, W. Siu, J. F. Pérez-Torres, F. Morales, G. Gademann, A. Rouzée, P. Johnsson, M. Lucchini, F. Calegari, J. L. Sanz-Vicario, F. Martín, and M. J. J. Vrakking, Phys. Rev. Lett. **107**, 043002 (2011).

[17] B. Fischer, M. Kremer, T. Pfeifer, B. Feuerstein, V. Sharma, U. Thumm, C.-D. Schröter, R. Moshammer, and J. Ullrich, Phys. Rev. Lett. **105**, 223001 (Nov. 2010), ISSN 0031-9007, http://link.aps.org/doi/10.1103/PhysRevLett.105.223001.

[18] M. Krüger, M. Schenk, and P. Hommelhoff, Nature **475**, 78 (Jul. 2011), ISSN 0028-0836, http://www.nature.com/doifinder/10.1038/nature10196.

[19] Y. H. Jiang, A. Rudenko, O. Herrwerth, L. Foucar, M. Kurka, K.-U. Kühnel, M. Lezius, M. F. Kling, J. van Tilborg, A. Belkacem, K. Ueda, S. Düsterer, R. Treusch, C.-D. Schröter, R. Moshammer, and J. Ullrich, Phys. Rev. Lett. **105**, 263002 (Dec. 2010), ISSN 0031-9007, http://link.aps.org/doi/10.1103/PhysRevLett.105.263002.

[20] F. H. M. Faisal, *Theory of Multiphoton Processes* (Plenum Press, New York, 1987).

[21] G. Sansone, E. Benedetti, F. Calegari, C. Vozzi, L. Avaldi, R. Flammini, L. Poletto, P. Villoresi, C. Altucci, R. Velotta, S. Stagira, S. De Silvestri, and M. Nisoli, Science **314**, 443 (2006).

[22] E. Goulielmakis, M. Schultze, M. Hofstetter, V. S. Yakovlev, J. Gagnon, M. Uiberacker, A. Aquila, E. M. Gullikson, D. T. Attwood, R. Kienberger, F. Krausz, and U. Kleineberg, Science **320**, 1614 (2008).

[23] P. G. Burke, P. Francken, and C. J. Joachain, J. Phys. B: At. Mol. Opt. Phys. **24**, 761 (1991).

[24] E. S. Smyth, J. S. Parker, and K. T. Taylor, Comp. Phys. Commun. **114**, 1 (1998).

[25] G. L. Kamta and A. F. Starace, Phys. Rev. A **65**, 053418 (2002).

[26] S. Laulan and H. Bachau, Physical Review A **69**, 033408 (Mar. 2004), ISSN 1050-2947, http://link.aps.org/doi/10.1103/PhysRevA.69.033408.

[27] J. L. Sanz-Vicario, H. Bachau, and F. Martín, Phys. Rev. A **73**, 033410 (2006).

[28] X.-M. Tong, K. Hino, and N. Toshima, Phys. Rev. A **74**, 031405(R) (Sep. 2006), ISSN 1050-2947, http://link.aps.org/doi/10.1103/PhysRevA.74.031405.

[29] E. Foumouo, G. L. Kamta, G. Edah, and B. Piraux, Phys. Rev. A **74**, 063409 (2006).

[30] P. Lambropoulos and L. A. A. Nikolopoulos, New J. Phys. **10**, 025012 (2008).

[31] M. A. Lysaght, P. G. Burke, and H. W. van der Hart, Phys. Rev. Lett. **101**, 253001 (2008).

[32] J. Feist, S. Nagele, R. Pazourek, E. Persson, B. I. Schneider, L. A. Collins, and J. Burgdörfer, Phys. Rev. A **77**, 043420 (Apr. 2008), ISSN 1050-2947, http://link.aps.org/doi/10.1103/PhysRevA.77.043420.

[33] A. Palacios, T. N. Rescigno, and C. W. McCurdy, Phys. Rev. A **77**, 032716 (Mar. 2008), ISSN 1050-2947, http://link.aps.org/doi/10.1103/PhysRevA.77.032716.

[34] R. Nepstad, T. Birkeland, and M. Førre, Phys. Rev. A **81**, 063402 (Jun. 2010), ISSN 1050-2947, http://link.aps.org/doi/10.1103/PhysRevA.81.063402.

[35] A. T. J. B. Eppink and D. H. Parker, Rev. Sci. Instrum. **68**, 3477 (1997).

[36] J. Ullrich, R. Moshammer, A. Dorn, R. D. Dörner,

L. P. H. Schmidt, and H. Schmidt-Böcking, Rep. Prog. Phys. **66**, 1463 (2003).

[37] E. Goulielmakis, Z.-H. Loh, A. Wirth, R. Santra, N. Rohringer, V. S. Yakovlev, S. Zherebtsov, T. Pfeifer, A. M. Azzeer, M. F. Kling, S. R. Leone, and F. Krausz, Nature **466**, 739 (Aug. 2010), ISSN 0028-0836, http://www.nature.com/doifinder/10.1038/nature09212.

[38] L. A. A. Nikolopoulos, T. K. Kjeldsen, and L. B. Madsen, Phys. Rev. A **75**, 063426 (Jun. 2007), ISSN 1050-2947, http://link.aps.org/doi/10.1103/PhysRevA.75.063426.

[39] T. K. Kjeldsen, L. B. Madsen, and J. P. Hansen, Phys. Rev. A **74**, 035402 (Sep. 2006), ISSN 1050-2947, http://link.aps.org/doi/10.1103/PhysRevA.74.035402.

[40] L. B. Madsen, L. A. A. Nikolopoulos, T. K. Kjeldsen, and J. Fernández, Phys. Rev. A **76**, 063407 (2007).

[41] F. Catoire and H. Bachau, Phys. Rev. A **85**, 023422 (Feb 2012), http://link.aps.org/doi/10.1103/PhysRevA.85.023422.

[42] C. W. McCurdy, M. Baertschy, and T. N. Rescigno, J. Phys. B: At. Mol. Opt. Phys. **37**, R137 (Sep. 2004), ISSN 0953-4075, http://stacks.iop.org/0953-4075/37/i=17/a=R01?key=crossref.2b47a7395a8201d53f3f3b2697689fbe.

[43] A. Palacios, C. W. McCurdy, and T. N. Rescigno, Phys. Rev. A **76**, 043420 (Oct. 2007), ISSN 1050-2947, http://link.aps.org/doi/10.1103/PhysRevA.76.043420.

[44] A. Palacios, T. N. Rescigno, and C. W. McCurdy, Phys. Rev. A **79**, 033402 (Mar. 2009), ISSN 1050-2947, http://link.aps.org/doi/10.1103/PhysRevA.79.033402.

[45] A. K. Kazansky, P. Selles, and L. Malegat, Phys. Rev. A **68**, 052701 (Nov. 2003), ISSN 1050-2947, http://link.aps.org/doi/10.1103/PhysRevA.68.052701.

[46] J. Fernández and L. B. Madsen, J. Phys. B: At. Mol. Opt. Phys. **42**, 085602 (Apr. 2009), ISSN 0953-4075, http://stacks.iop.org/0953-4075/42/i=8/a=085602?key=crossref.dd08a12f4c22eab66e8a422af0f4b69d.

[47] L. Tao and A. Scrinzi, New Journal of Physics **14**, 013021 (2012), http://stacks.iop.org/1367-2630/14/i=1/a=013021.

[48] A. Scrinzi, New Journal of Physics **14**, 085008 (2012), http://stacks.iop.org/1367-2630/14/i=8/a=085008.

[49] J. Feist, *Two-photon double ionization of helium*, Ph.D. thesis, Vienna Univ. of Technology (2009).

[50] B. I. Schneider, J. Feist, S. Nagele, R. Pazourek, S. X. Hu, L. A. Collins, and J. Burgdörfer, in *Quantum Dynamic Imaging*, CRM Series in Mathematical Physics, edited by A. D. Bandrauk and M. Ivanov (Springer, 2011) Chap. 10.

[51] J. Colgan and M. S. Pindzola, Phys. Rev. Lett. **88**, 173002 (2002).

[52] S. Laulan and H. Bachau, Phys. Rev. A **68**, 013409 (Jul. 2003).

[53] S. X. Hu, J. Colgan, and L. A. Collins, J. Phys. B **38**, L35 (2005).

[54] M. S. Pindzola, F. Robicheaux, S. D. Loch, J. C. Berengut, T. Topcu, J. Colgan, M. Foster, D. C. Griffin, C. P. Ballance, D. R. Schultz, T. Minami, N. R. Badnell, M. C. Witthoeft, D. R. Plante, D. M. Mitnik, J. A. Ludlow, and U. Kleiman, J. Phys. B **40**, R39 (2007).

[55] T. N. Rescigno and C. W. McCurdy, Phys. Rev. A **62**, 032706 (2000).

[56] C. W. McCurdy, D. A. Horner, and T. N. Rescigno, Phys. Rev. A **63**, 022711 (2001).

[57] B. I. Schneider, L. A. Collins, and S. X. Hu, Phys. Rev. E **73**, 036708 (2006).

[58] T. J. Park and J. C. Light, J. Chem. Phys. **85**, 5870 (1986).

[59] E. S. Smyth, J. S. Parker, and K. T. Taylor, Comput. Phys. Commun. **114**, 1 (Nov. 1998).

[60] C. Leforestier, R. H. Bisseling, C. Cerjan, M. D. Feit, R. Friesner, A. Guldberg, A. Hammerich, G. Jolicard, W. Karrlein, H.-D. Meyer, N. Lipkin, O. Roncero, and R. Kosloff, J. Comp. Phys. **94**, 59 (1991).

[61] V. Hernandez, J. E. Roman, and V. Vidal, ACM Trans. Math. Softw. **31**, 351 (Sep. 2005).

[62] R. G. Newton, *Scattering Theory of Waves and Particles* (McGraw-Hill, New York, 1966).

[63] G. Breit and H. A. Bethe, Phys. Rev. **93**, 888 (Feb 1954), http://link.aps.org/doi/10.1103/PhysRev.93.888.

[64] S. Altshuler, Il Nuovo Cimento (1955-1965) **3**, 246 (1956).

[65] J. T. Broad and W. P. Reinhardt, Phys. Rev. A **14**, 2159 (1976).

[66] M. L. Du and A. Dalgarno, Phys. Rev. A **43**, 3474 (1991).

[67] I. Bray, D. A. Konovalov, and I. E. McCarthy, Phys. Rev. A **43**, 1301 (1991).

[68] R. Moccia and P. Spizzo, Phys. Rev. A **43**, 2199 (Mar 1991), http://link.aps.org/doi/10.1103/PhysRevA.43.2199.

[69] I. Sánchez and F. Martín, Phys. Rev. A **44**, 13(R) (1991).

[70] P. G. Burke, *R-Matrix Theory of Atomic Collisions* (Springer-Verlag, Heidelberg, 2011).

[71] W. Vanroose, J. Broeckhove, and F. Arickx, Phys. Rev. Lett. **88**, 010404 (Dec. 2001), ISSN 0031-9007, http://link.aps.org/doi/10.1103/PhysRevLett.88.010404.

[72] I. Cacelli, V. Carravetta, A. Rizzo, and R. Moccia, Phys. Rep. **205**, 283 (1991).

[73] L. Argenti and R. Moccia, J. Phys. B: At. Mol. Opt. Phys. **39**, 2773 (2006).

[74] F. Martín, Phys. Rev. A **48**, 331 (1993).

[75] M. Venuti, P. Decleva, and A. Lisini, J. Phys. B: At. Mol. Opt. Phys. **29**, 5315 (1996).

[76] S. Balay, J. Brown, K. Buschelman, W. D. Gropp, D. Kaushik, M. G. Knepley, L. C. McInnes, B. F. Smith, and H. Zhang, "PETSc Web page," (2011).

[77] M. Brauner, J. S. Briggs, and H. Klar, J. Phys. B: At. Mol. Opt. Phys. **22**, 2265 (1989).

[78] G. W. F. Drake, G. A. Victor, and A. Dalgarno, Phys. Rev. **180**, 25 (1969).

[79] J. M. Rost, K. Schulz, M. Domke, and G. Kaindl, Journal of Physics B: Atomic, Molecular and Optical Physics **30**, 4663 (1997), http://stacks.iop.org/0953-4075/30/i=21/a=010.

[80] G. Tanner, K. Richter, and J. M. Rost, Rev. Mod. Phys **72**, 497 (2000).

[81] M. Domke, C. Xue, A. Puschmann, T. Mandel, E. Hudson, D. A. Shirley, G. Kaindl, C. H. Greene, H. R. Sadeghpour, and H. Petersen, Phys. Rev. Lett. **66**, 1306 (Mar. 1991).

[82] J. M. Bizau, F. Wuilleumier, P. Dhez, D. L. Ederer, T. N. Chang, S. Krummacher, and V. Schmidt, Phys. Rev. Lett. **48**, 588 (Mar. 1982).

[83] I. Sánchez and F. Martín, Phys. Rev. A **44**, 7318 (Dec. 1991).

[84] I. Sánchez and F. Martín, Phys. Rev. A **45**, 4468 (Apr. 1992).

[85] A. Menzel, S. P. Frigo, S. B. Whitfield, C. D. Caldwell, and M. O. Krause, Phys. Rev. A **54**, 2080 (Sep. 1996).

[86] M. Zubek, G. Dawber, R. I. Hall, L. Avaldi, K. Ellis, and G. C. King, J. Phys. B **24**, L337 (Jan. 1999).

[87] D. W. Lindle, T. A. Ferrett, U. Becker, P. H. Kobrin, C. M. Truesdale, H. G. Kerkhoff, and D. A. Shirley, Phys. Rev. A **31**, 714 (Feb. 1985).

[88] M. Venuti, P. Decleva, and A. Lisini, J. Phys. B **29**, 5315 (Jan. 1999).

[89] I. Sánchez and F. Martín, Phys. Rev. A **47**, 1520 (Feb 1993), http://link.aps.org/doi/10.1103/PhysRevA. 47.1520.

[90] T. K. Fang and T. N. Chang, Phys. Rev. A **61**, 062704 (May 2000).

[91] B. Zhou and C. D. Lin, Phys. Rev. A **49**, 1057 (Feb. 1994).

[92] M. Alagia, M. Coreno, H. Farrokhpour, P. Franceschi, A. Mihelič, A. Moise, R. Omidyan, K. C. Prince, R. Richter, J. Söderström, S. Stranges, M. Tabrizchi, and M. Žitnik, Phys. Rev. Lett. **102**, 153001 (Apr. 2009), ISSN 0031-9007, http://link.aps.org/doi/10. 1103/PhysRevLett.102.153001.

[93] C. D. Lin, Adv. At. Mol. Phys. **22**, 77 (1986).

[94] C. D. Lin, Phys. Rev. A **29**, 1019 (Mar. 1984).

[95] D. R. Herrick, M. E. Kellman, and R. D. Poliak, Phys. Rev. A **22**, 1517 (Oct. 1980).

[96] J. M. Feagin and J. S. Briggs, Phys. Rev. Lett. **57**, 984 (Aug. 1986).

[97] D. R. Herrick and O. Sinanoğlu, Phys. Rev. A **11**, 97 (Jan. 1975).

[98] U. Fano, Phys. Rev. **124**, 1866 (Dec 1961), http:// link.aps.org/doi/10.1103/PhysRev.124.1866.

[99] M. Wickenhauser, J. Burgdörfer, F. Krausz, and M. Drescher, Phys. Rev. Lett. **94**, 023002 (2005).

[100] M. Wickenhauser, Burgdörfer, F. Krausz, and M. Drescher, J. Mod. Opt. **53**, 247 (Jan. 2006).

[101] M. Wickenhauser, *Ionization dynamics of atoms in femto- and attosecond pulses*, Ph.D. thesis, Vienna Univ. of Technology (2006).

[102] J. Mauritsson, T. Remetter, M. Swoboda, K. Klünder, A. L'Huillier, K. J. Schafer, O. Ghafur, F. Kelkensberg, W. Siu, P. Johnsson, M. J. J. Vrakking, I. Znakovskaya, T. Uphues, S. Zherebtsov, M. F. Kling, F. Lépine, E. Benedetti, F. Ferrari, G. Sansone, and M. Nisoli, Phys. Rev. Lett. **105**, 053001 (Jul. 2010).

[103] C. Ott, A. Kaldun, P. Raith, K. Meyer, M. Laux, Y. Zhang, S. Hagstotz, T. Ding, R. Heck, and T. Pfeifer, arXiv [physics.atom-ph] **05**, 0519v1 (2012).

[104] L. Argenti, C. Ott, T. Pfeifer, and F. Martín, arXiv [physics.atom-ph] **11**, 1211.2566v1 (2012).

[105] K. L. Ishikawa and K. Midorikawa, Phys. Rev. A **72**, 013407 (2005).

[106] A. Palacios, D. A. Horner, T. N. Rescigno, and C. W. McCurdy, J. Phys. B **43**, 194003 (Sep. 2010).

[107] R. Pazourek, J. Feist, S. Nagele, E. Persson, B. I. Schneider, L. A. Collins, and J. Burgdörfer, Phys. Rev. A **83**, 053418 (May 2011).

[108] H. Bachau, E. Cormier, P. Decleva, J. E. Hansen, and F. Martín, Rep. Prog. Phys. **64**, 1815 (2001).

[109] L. Argenti and R. Colle, Comp. Phys. Commun. **180**, 1442 (Sep. 2009), ISSN 00104655, http://linkinghub. elsevier.com/retrieve/pii/S0010465509000848.

[110] L. Argenti and R. Moccia, J. Phys. B: At. Mol. Opt. Phys. **41**, 035002 (Feb. 2008), ISSN 0953-4075, http: //stacks.iop.org/0953-4075/41/i=3/a=035002?key= crossref.5ab2921b96d1d4c22b002a1e537e96d7.

[111] L. Argenti and R. Moccia, J. Phys. B: At. Mol. Opt. Phys. **43**, 235006 (2010).

[112] E. Lindroth and L. Argenti, Adv. Q. Chem. **63**, 247 (2012).
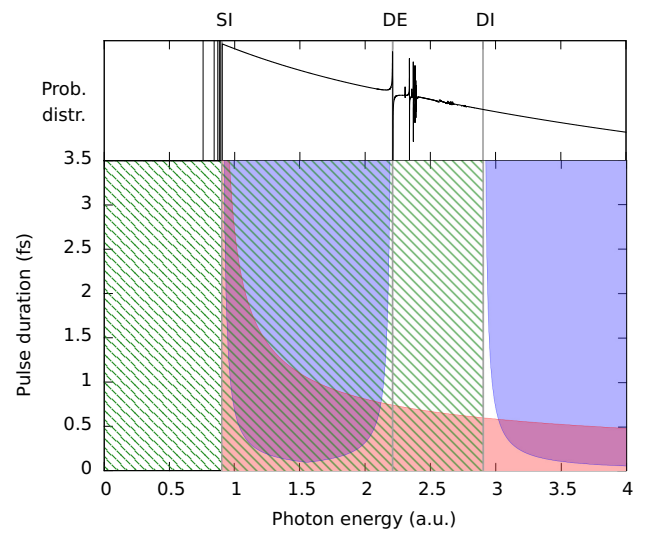
FIGURES

FIG. 1. (Color online) Approximate regions of applicability of different extraction methods for the single ionization continuum of helium as a function of photon energy and pulse duration for a single-photon transition. SI: single ionization, DE: double excitation, DI: double ionization. Green shaded: projection on scattering states (PSS), blue solid: projection onto asymptotic channel functions, red solid: Berkeley-ECS method. See text for details. The upper part shows the (logarithmic) ionization probability for single ionization and positions of excited bound states.
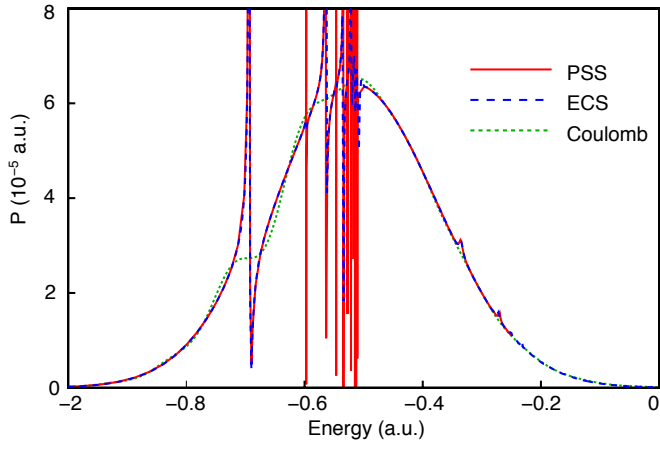
FIG. 2. (Color online) Photoelectron distribution in the $1s$ $^1\mathrm{P}^o$ channel resulting from the photoionization of helium from the ground state with an XUV pulse with $\omega = 2.4$ a.u., $I = 10^{12}\mathrm{W/cm}^2$, and $T_{\mathrm{FWHM}}=200$ as. Projection onto scattering states (PSS), red solid line; Berkeley-ECS, blue dashed line; projection on the product of Coulomb functions at $t = 1000$ as after the center of the XUV pulse, green dotted line.
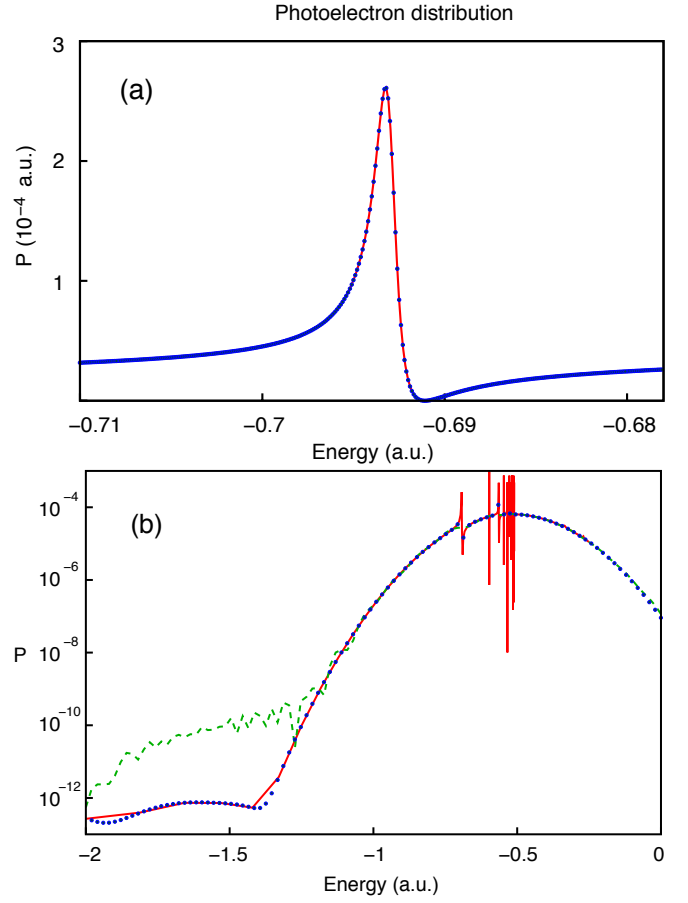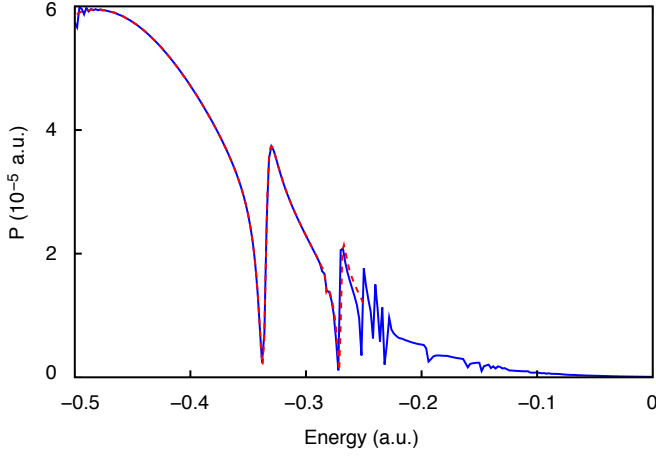

FIG. 3. (Color online) Photoelectron spectrum as in Fig. 2 with (a) a close-up near the sp_2^+ resonance, and (b) the spectrum on a logarithmic scale to highlight small deviations in the tails of the direct ionization peak.

FIG. 4. (Color online) Photoelectron distribution in the $N = 2$ $^1P^o$ channel resulting from the photoionization of helium from the ground state with an XUV pulse with $\omega = 2.4$ a.u., $I = 10^{12}$ W/cm^2, and $T_{\mathrm{FWHM}}=200$ as. PSS: red dashed line; ECS: blue solid line.
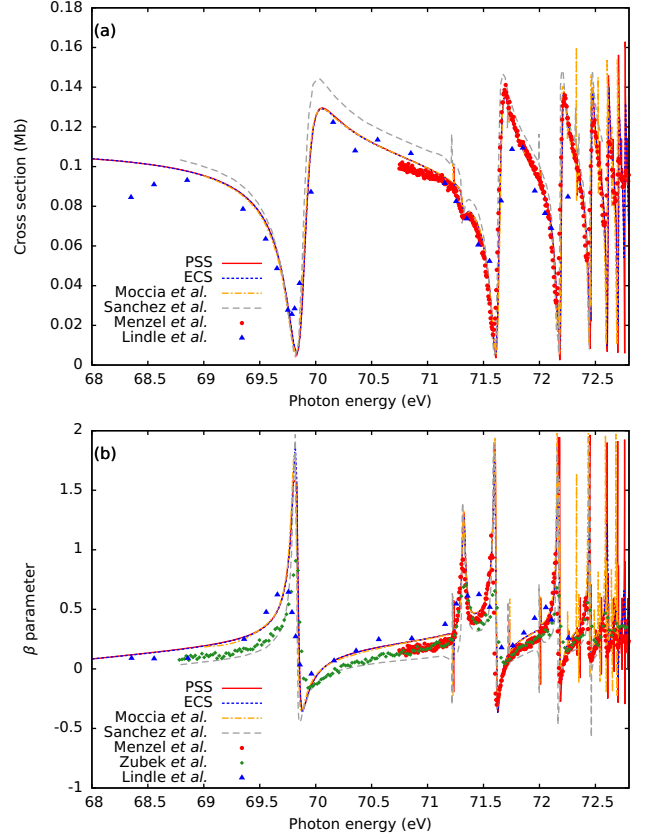

FIG. 5. (Color online) Photoionization cross section $\sigma_2(\omega)$ (Eq. 22) and anisotropy parameter β_2 (Eq. 25) for ionization of helium from the ground state to N=2 excited ionic states, in the region of autoionizing resonances between the N=2 and the N=3 thresholds. We compare our results obtained by the Berkeley-ECS and PSS methods with the theoretical values in velocity gauge by Moccia and Spizzo [68], earlier theoretical values by Sanchez et al. , [83] and [84] and experimental results by Menzel et al [85], Zubek et al [86] and Lindle et al [87]. Our results agree perfectly with the theoretical values of Moccia et al. (and with results by Venuti et al [88], not shown) and are in best agreement with the experimental data of Lindle et al.

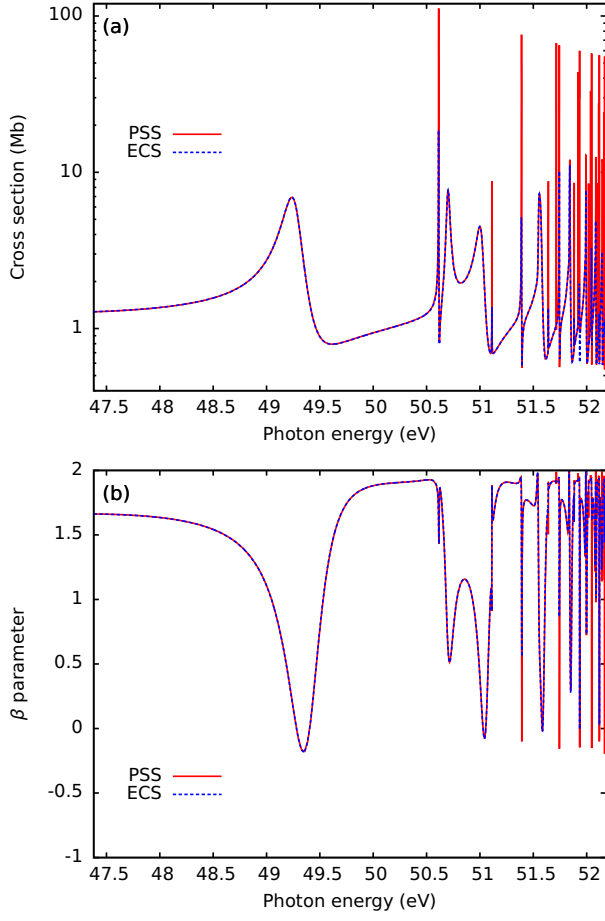FIG. 6. (Color online) Photoionization cross section and anisotropy parameter β_2 between the N=2 and the N=3 thresholds for ionization of helium from the metastable ^{1}S ($1s2s$) state. PSS: red solid line; ECS: blue dotted line.
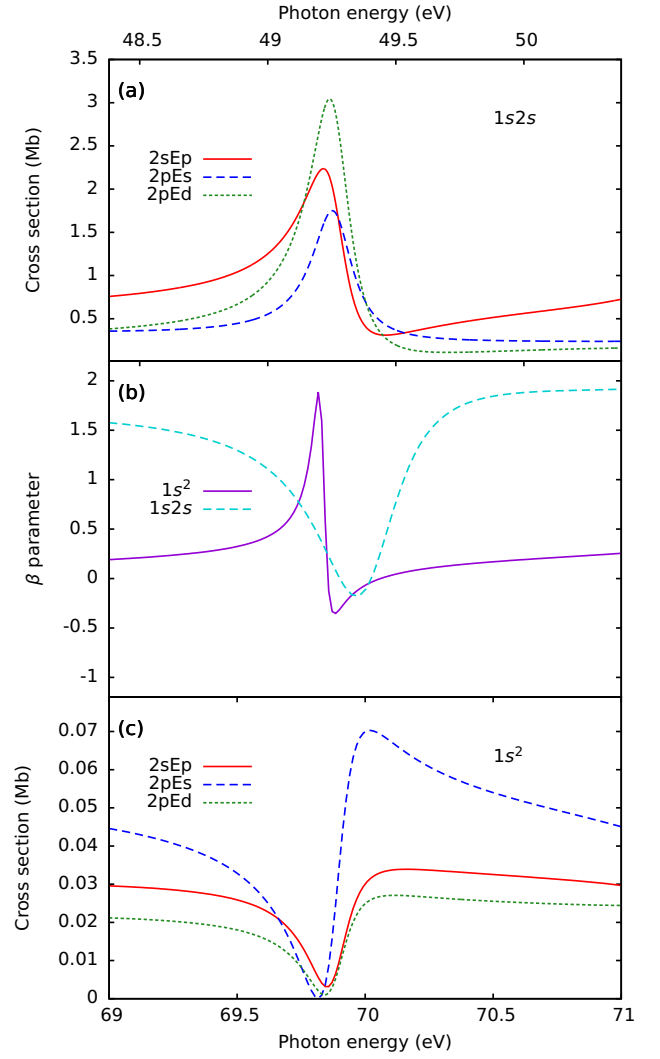

FIG. 7. (Color online) Partial $N=2$ photoionization cross sections for the first ^{1}P^o autoionizing resonance below the $N=3$ threshold for ionization from the metastable ^{1}S ($1s2s$) state (a) and ionization from the ground state (c). In (b) the according β_2 parameters for $n=2$ are compared, where the energies are shifted such that the resonance appears at the same position. The lower energy axis corresponds to ionization from the ground state, while the upper energy axis corresponds to ionization from the metastable ^{1}S ($1s2s$) state.

FIG. 9. (Color online) Close-up of the evolution of the photoelectron spectrum determined by projection on products of Coulomb functions in comparison with the asymptotic Fano profile extracted from the same wavepacket by projection onto scattering states immediately after the end of the external pulse.
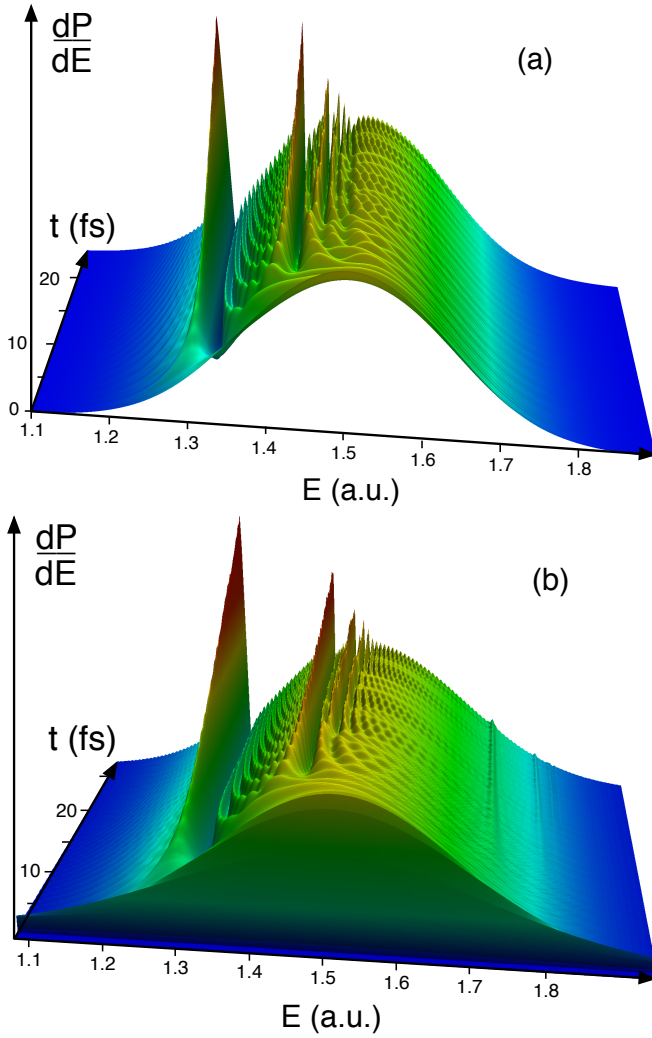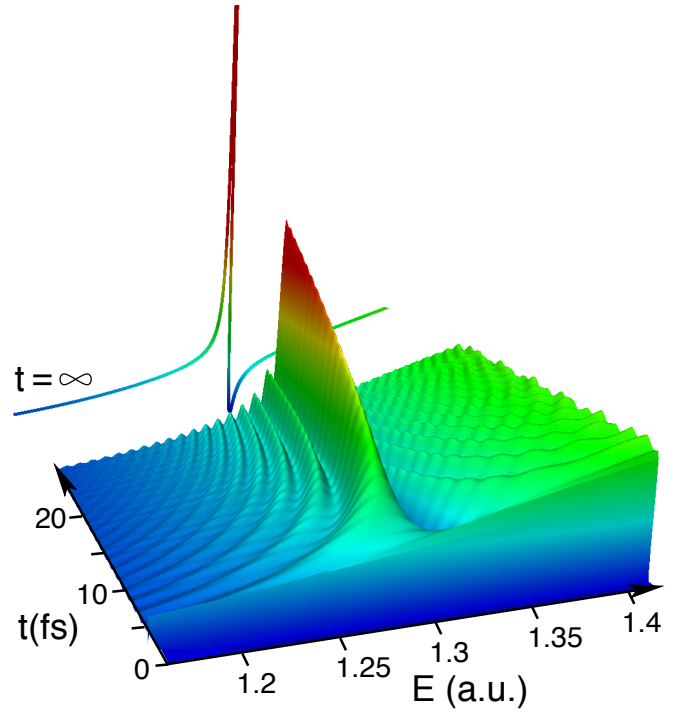
FIG. 8. (Color online) a) Formation of the Fano profiles for a regular series of autoionizing Rydberg states according to the Fano model within the impulsive approximation. The energy distribution of the photoelectron is multiplied by a Gaussian spectral-shape function to simulate the effect of an attosecond pulse. This approach is justified as long as the duration of the pulse is much shorter than the lifetimes of the autoionizing states. See text for more details.

b) Total photoelectron spectrum of the wavepacket created by the action of a sub-femtosecond pulse on the ground state of the helium atom and computed by projecting the wavepacket on products of bound ($Z=2$) and continuum ($Z=1$) Coulomb functions. Since such products are not eigenstates of the field-free Hamiltonian, the spectrum is only approximated and changes with time after the XUV pulse. As the doubly excited states populated by the pulse decay, characteristic Fano profiles build up. See text for more details.

FIG. 11. (Color online) Singly differential photoelectron distribution after two-photon double ionization of helium by a sub-femtosecond XUV pulse ($\omega = 2.4$ a.u., $I = 10^{12}$ W/cm^2, and $T_{\mathrm{FWHM}} = 200$ as). Two different extraction methods are compared: projection on products of Coulomb functions with $Z = 2$ performed 1 fs (red dashed line) and 7 fs (black solid line) after the peak of the XUV pulse and the Berkeley-ECS method (green dotted line) for a computational box with $R = 244$ a.u. performed 1 fs after the peak of the XUV pulse.
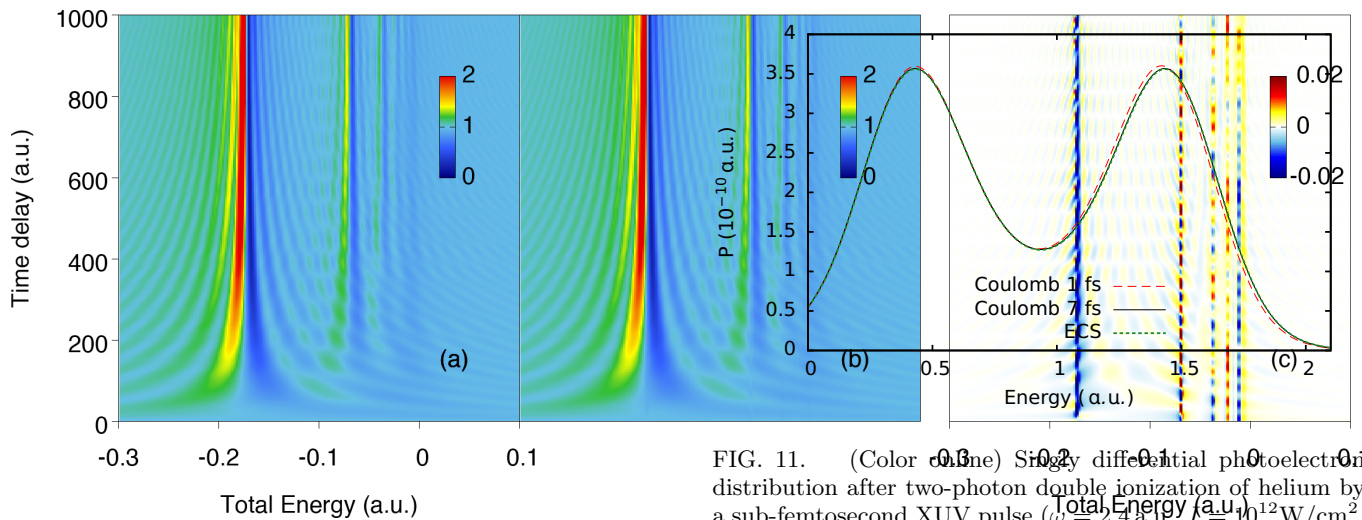
FIG. 10. (Color online) a) Time evolution of the photoelectron distribution, $P(E, t)$, in the unperturbed continuum as a function of time after the impulsive excitation of a series of autoionizing resonances. b) Asymptotic photoelectron distribution $\bar{P}(E, \tau)$ as a function of the time delay τ between the impulsive excitation and the impulsive depletion of the residual localized part of the autoionizing resonances. c) shows the comparatively small differences that exist between the two spectra.
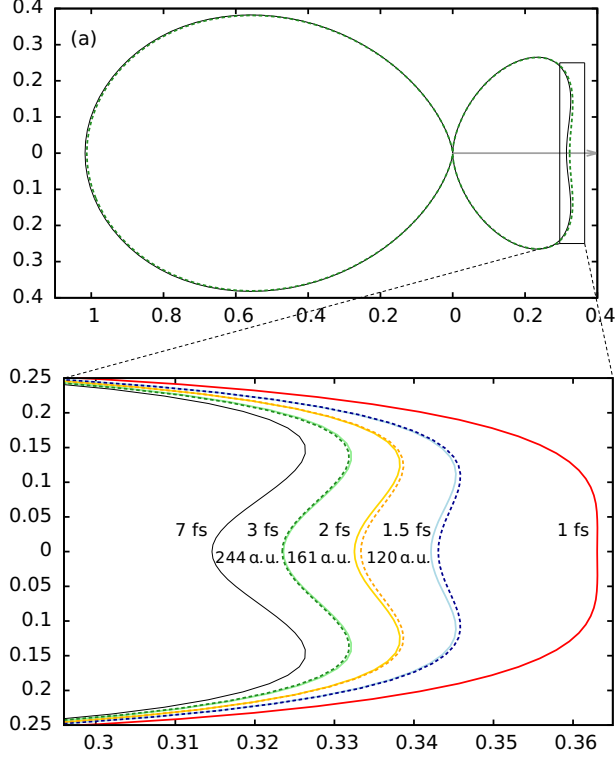
FIG. 12. (Color online) Conditional angular distribution for one electron emitted in the laser polarization axis [grey arrow in (a)] and integrated over both electron energies after two-photon double ionization of helium by a sub-femtosecond XUV pulse ($\omega = 2.4$ a.u., $I = 10^{12}$ W/cm^2, and $T_{\mathrm{FWHM}}=200$ as). Two different extraction methods are compared (a): projection on products of Coulomb functions with $Z = 2$ performed 7 fs (black solid line) after the peak of the XUV pulse and the Berkeley-ECS method (green dotted line) for an extraction radius of $R = 244$ a.u. performed 1 fs after the peak of the XUV pulse. In (b) a close-up of the emission of the two electrons in the same direction is shown, illustrating the convergence of the Berkeley-ECS method with extraction radius (dotted lines) and of the Coulomb projection with propagation time (solid lines). The two techniques agree when the extraction radius of the Berkeley-ECS method approximately equals the position (of the relevant parts) of the wavepacket at the time of projection on the Coulomb functions. The partial wave expansion includes angular momenta up to $l_1 = l_2 = 15$.

TABLE I. Comparison between the energies of the He Rydberg states with principal quantum number for the outer electron up to $n = 6$, obtained by diagonalizing the Hamiltonian in either the FEDVR (upper value, $R = 156$ a.u.) or the B-spline (lower value, $R=800$ a.u.) basis.

n	$^1\mathrm{S}^e$	Symmetry $^1\mathrm{P}^o$	$^1\mathrm{D}^e$
1	-2.903 5102		
	-2.903 5164		
2	-2.145 9610	-2.123 8231	
	-2.145 9615	-2.123 8232	
3	-2.061 2684	-2.055 1399	-2.055 6203
	-2.061 2685	-2.055 1400	-2.055 6203
4	-2.033 5852	-2.031 0669	-2.031 2796
	-2.033 5853	-2.031 0669	-2.031 2796
5	-2.021 1761	-2.019 9046	-2.020 0016
	-2.021 1761	-2.019 9045	-2.020 0016
6	-2.014 5627	-2.013 8331	-2.013 8981
	-2.014 5627	-2.013 8331	-2.013 8981

TABLE II. Error in the norm of the bound states translated from the B-spline to the FEDVR basis $\tilde{\delta}_n = 1 - \langle \tilde{\phi}_n | \tilde{\phi}_n \rangle$, and error in the overlap $\delta_n = 1 - \langle \phi_n | \tilde{\phi}_n \rangle$ (see text for details). The notation $[n]$ is a shorthand for 10^{-n}.

n	$^1\mathrm{S}$ $\tilde{\delta}_n$	δ_n	$^1\mathrm{P}^o$ $\tilde{\delta}_n$	δ_n	$^1\mathrm{D}^e$ $\tilde{\delta}_n$	δ_n
1	8.0[-7]	8.2[-7]				
2	7.6[-8]	7.8[-8]	7.4[-11]	3.9[-10]		
3	2.4[-8]	2.5[-8]	2.5[-9]	2.7[-9]	3.3[-9]	3.3[-9]
4	1.2[-8]	2.1[-8]	3.0[-9]	1.3[-8]	3.3[-9]	9.8[-9]
5	7.6[-9]	1.7[-8]	3.1[-9]	1.1[-8]	3.3[-9]	1.3[-8]
6	6.1[-9]	1.3[-8]	4.7[-9]	1.6[-8]	4.0[-9]	1.3[-8]